PHYSICAL REVIEW B VOLUME 26, NUMBER 2 15 JULY 1982

Strain-confined electron-hole liquid in Ge: Density variations and compressibility

S. M. Kelso*
Physics Department, University of California, Berkeley, California 94720
and Materials and Molecular Research Division, Lawrence Berkeley Laboratory,
Berkeley, California 94720
(Received 22 February 1982)

We present a detailed theoretical and experimental investigation of a spatial variation in the electron-hole—pair density in the strain-confined electron-hole liquid in Ge. The density variation can be dramatic: We observed a compression of the central density by a factor of 3 for our largest drop radius, $R \approx 0.7$ mm. Our experimental density profiles, obtained using Abel transforms of spatial luminescence profiles, are in good agreement with the theoretical predictions of approximately parabolic profiles with densities larger than the equilibrium value at the center of the drop. Our previous first-order theory has been extended to include the full density dependence of the pair free energy at finite stress and temperature. We discuss the shape and power dependence of spatial luminescence profiles and luminescence spectra, since the spatial density variation increases with drop size. We use the central densities for drop sizes ranging over an order of magnitude to measure the density dependence of the electron-hole—liquid chemical potential, providing a sensitive test of many-body theories for the correlation energy. We obtain an improved value for the isothermal compressibility of the strain-confined liquid: $K_T = 0.067 \pm 0.017$ cm^2/dyn for $n = 0.47 \times 10^{17}$ cm^{-3}, $T = 1.9$ K, and $-\sigma = 5.5$ kgf/mm^2, where kgf represents kilogram force.

I. INTRODUCTION

Since the discovery of electron-hole drops over ten years ago, an enormous variety of experimental and theoretical studies have been performed to elucidate the properties of electron-hole liquids (EHL) in semiconductors.[1,2] Several years ago, microwave experiments[3,4] in Ge indicated the formation of a new type of EHL having a drop size of hundreds of μm and a lifetime of hundreds of μsec. The experiments were performed using a so-called Hertzian stressing geometry, in which the shear strain maximum and its associated electron-hole—pair energy minimum occur in the interior of the crystal, well separated from the surfaces.[5] Pairs collect in the strain well and coalesce to form a single drop of liquid, which we denote the strain-confined electron-hole liquid (SCEHL).

Many experiments have been performed to learn the properties of the SCEHL. Among them are luminescence,[6–13] microwave resonance,[3,4,14,15] microwave conductivity,[16,17] far-infrared absorption,[15,18,19] and ultrasonic attenuation[20] studies. The electron-hole—pair density has been measured using several techniques[11,16,20–22] and is $\sim 0.5 \times 10^{17}$ cm^{-3} for stresses ~ 5 kgf/mm^2 (where kgf stands for kilogram force), considerably reduced from the value for unstressed Ge due to the changes in the band structure.[1,2] The lifetime is longer, as a result of the reduced density; several experiments[4,7,11,12,15,16] give results of ~ 500 μsec. The binding energy with respect to free excitons, φ, is approximately 1 meV (Refs. 11 and 23) and the critical temperature $T_c \sim 5-6$ K.[15,23] The formation of the liquid,[14] the kinetics of the surrounding excitons[15] and free carriers,[16,24] and eddy currents within the liquid[25] have also been studied.

The interpretation of our experimental results relies on the formation of a single electron-hole drop (EHD) in inhomogeneously strained Ge. There is much evidence to support this.[26] For example, in light-scattering experiments[21,22] the large-angle scattering typical of Rayleigh-Gans scattering by small drops[27,28] vanished. In addition, Alfvén resonances[3,4,15,29] occur when the drop diameter is matched to a multiple of the microwave wavelength inside the drop. The Alfvén waves require a continuous medium in which to propagate. Further evidence for a single drop is its distortion in an external magnetic field.[8,9] This magnetostric-

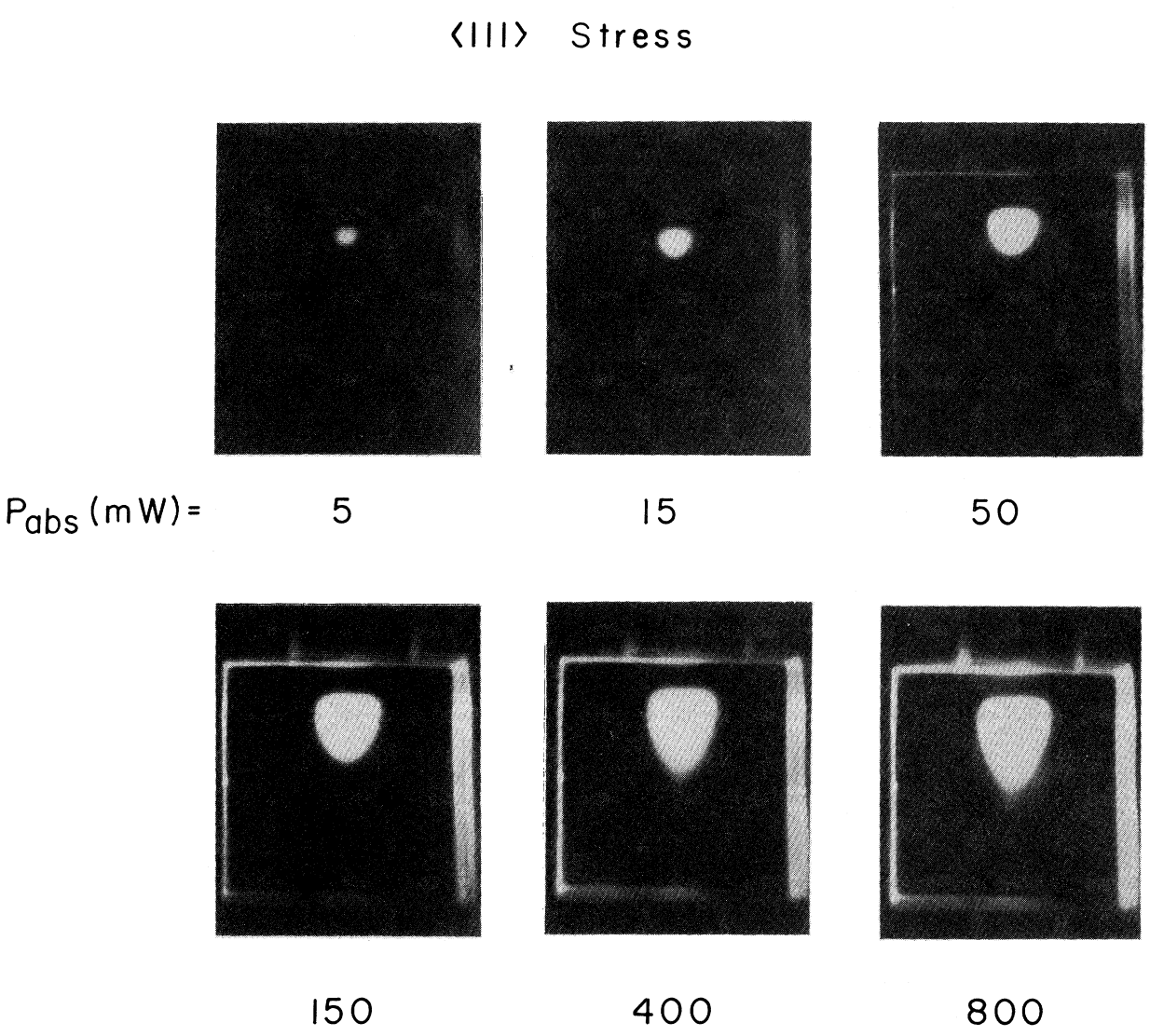

FIG. 1. Photographs of luminescence images from a Ge crystal inhomogeneously stressed in the ⟨111⟩ direction. The images are displayed using an infrared vidicon and standard television monitor (Ref. 6). The excitation levels are given by the absorbed laser power, P_{abs}. $T=1.8$ K.

tion arises from the recombination currents set up by decaying pairs in a single macroscopic drop.[30] The observations of much brighter luminescence intensity as compared to unstressed crystals[11] and the decay of the spatial extent after excitation cutoff[4,11] also indicate the formation of a single drop in the strain well.

The drop size depends on the excitation level. Figure 1 shows a series of photographs[6] of the luminescence emitted at $\lambda \approx 1.75$ μm by the SCEHL in a ⟨111⟩-stressed sample. The excitation levels are denoted by the absorbed laser power P_{abs}. At low excitation, an approximately spherical drop forms at the bottom of the potential well. At higher excitation levels, the drop becomes nonspherical as its shape conforms to a surface of constant strain energy. The largest drop in the figure has a diameter of ~ 1.4 mm and a volume of ~ 1.5 mm^3, making it the largest EHD studied to date.

In a previous paper,[11] properties of the SCEHL such as its size, spectral linewidth, and lifetime

were studied as a function of excitation level. For small drop sizes the stress is nearly uniform, and the equilibrium EHL properties for uniaxial stress may be studied. As the drop grows larger, the strain gradient becomes more important. The observed increase in the linewidth and decrease in the lifetime indicate that the liquid becomes compressed. A simple theory was developed[31] which predicted a variation in the electron-hole—pair density with position within the drop, and in preliminary experiments[10] density profiles of the predicted form were measured. The density variations were exploited to give a preliminary measurement of the compressibility of the SCEHL (Ref. 13) and to study the density dependence and relative importance of different recombination mechanisms.[12] Later, luminescence and microwave conductivity measurements showed an increase in the average density with drop size.[17]

In this paper we investigate in detail the compression of the SCEHL, both theoretically and experimentally. We present additional qualitative evidence for compression from luminescence imaging experiments. The density variation can be explained theoretically in a straightforward manner by assuming that the SCEHL is in diffusive equilibrium, i.e., that the chemical potential is a constant throughout the drop volume. We extend our previous theory,[31] which is valid for a restricted range of conditions around the ground state, to include the full density dependence of the electron-hole—pair free energy at finite stress and temperature. We find, as previously, that the density is larger at the center of the drop than at the surface, with an approximately parabolic variation with position. The density at the surface should remain approximately the equilibrium density n_0 for the stress at the bottom of the well, due to the slow variation in n_0 with uniaxial stress, while increases in the central density of a factor of 3 should be readily attainable in experiments. Thus, a unique feature of the SCEHL in Ge (Ref. 26) is that the density changes as the liquid is squeezed by the strain well at a fixed temperature.

We also discuss the effects of the spatial density variation on the shape of spatial luminescence profiles as a function of drop size. We show that density profiles can be obtained from Abel transforms of luminescence profiles obtained by scanning the crystal image across a small aperture. The density variations we measure for drop sizes ranging over an order of magnitude are in good agreement with the predictions, both in form and in magnitude. We use the central densities to determine experimentally the density dependence of the EHL chemical potential. This provides a sensitive test of the many-body theories used to describe correlations in electron-hole liquids. While the measurements differ from the particular theory we consider, we believe the discrepancy may lie within the uncertainty in the mathematical representation of that theory. We use the density-dependent chemical potential to obtain a refined value for the isothermal compressibility K_T of the SCEHL: $K_T=0.067 \pm 0.017$ cm^2/dyn for $n=0.47\times10^{17}$ cm^{-3}, $T=1.9$ K, and $-\sigma=5.5$ kgf/mm^2. This value is nearly 30 times greater than in unstressed Ge. Equipped with an accurate description of the density variation for different drop sizes, we discuss the spectral line shape expected from a drop having such a density profile. Several features of our calculated composite spectra are in good agreement with experiment.

This paper is divided into a number of sections. In Sec. II we discuss some experimental details. The strain well is characterized in Sec. III. Qualitative evidence for the compression of the SCEHL is presented in Sec. IV. In Sec. V, we review the first-order theory of the density variation and present an exact theory. The manifestation of the density variation in spatial luminescence profiles is discussed in Sec. VI. We present experimental density profiles in Sec. VII. The density dependence of the chemical potential and the compressibility are considered in Sec. VIII. Finally, in Sec. IX we discuss composite luminescence spectra.

II. EXPERIMENTAL DETAILS

The sample used in the experiments was cut from a large single crystal of ultrapure dislocation-free Ge grown by Hansen and Haller.[32] The material is uncompensated, i.e., $(N_A+N_D)/|N_A-N_D| \lesssim 10$, with a net impurity concentration $|N_A-N_D| \lesssim 10^{11}$ cm^{-3}. The primary electrically active impurity is an acceptor level at ~ 80 meV with a concentration $\sim 2\times10^{11}$ cm^{-3} which is believed to be due to hydrogen-divacancy complexes.[33] The sample was cut along crystal symmetry axes, lapped, etched in a $3HNO_3$:HF solution, and rinsed with methanol. Its final dimensions were $3.85\times3.95\times2.80$ mm^3 measured parallel to the $\langle 111\rangle$, $\langle 11\bar{2}\rangle$, and $\langle 1\bar{1}0\rangle$ directions, respectively.

The sample was mounted in the holder shown in

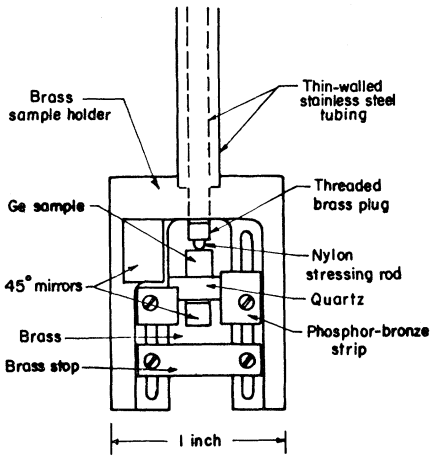

FIG. 2. Diagram of sample holder, showing the arrangement for stressing a Ge sample and for viewing it from three mutually perpendicular directions. The diagram is to the scale shown.

Fig. 2, sitting on a flat quartz plate, and was stressed along the ⟨111⟩ direction by a nylon rod with a rounded tip. This geometry results in the formation of a single strain well in the interior of the sample.[5] The force on the nylon plunger was transmitted by a stainless-steel tube from a calibrated spring arrangement outside the cryostat. The sample was stressed at room temperature before cooling to liquid-helium temperatures. We selected a carefully machined plunger with a large radius of curvature to obtain a contact area $\gtrsim 2$ mm^2. Because of the large contact area and sample thickness, the strain well was unusually large and well separated from all surfaces of the crystal. The holder in Fig. 2 was equipped with front-surface mirrors oriented at 45° located below and next to the sample to permit viewing from three mutually perpendicular directions.

The setup was similar to that used previously,[11] with a few additions and modifications. To ensure that the laser output remained stable throughout a series of scans, up to a few hours in duration, we used a stabilizer circuit[34] added to the power supply. Using this circuit and neutral density filters, the laser excitation was varied by nearly 5 orders of magnitude. The laser output was square-wave modulated at ~ 85 Hz. The relatively long pulse length (~ 5.9 msec) reduced the effect of phase shifts due to different luminescence decay times from different regions of the drop. Signal averaging was provided by a PAR model 186A synchronous lock-in amplifier, whose output was fed into an 8-bit analog-to-digital converter and punched onto paper tape. The tapes were later processed by computer.

The luminescence was detected by a cooled reverse-biased PIN photodiode fabricated from ultrapure single-crystal Ge by Haller using a procedure outlined in Ref. 32. A bias voltage of -180 V depleted the entire device. The detector was continuously maintained in vacuum at its operating temperature ($T \sim 160$ K) to reduce hydrocarbon and water contamination of the surfaces and to minimize thermal cycling. The operating temperature was chosen[35] to maximize the signal-to-noise ratio by nearly matching the indirect band gap while reducing the total noise from the thermally generated dark current and the first amplification stage. We estimate a quantum efficiency of $\sim 37\%$ under operating conditions. The change in detector response with wavelength was included in the fits of the spectra in Figs. 6 and 23.

The detector was connected to a current amplifier with a response time of 10 μsec. The luminescence intensity is conveniently expressed as the amplifier output in mV, where 1 mV corresponds to 3.0×10^{-10} W incident on the detector or 2.5×10^{-5} W radiated by the EHL.[35] The detector output was quite reproducible: The daily normalization factor varied by only $\sim 25\%$ over several weeks of experiments.

Our imaging technique was crucial in obtaining detailed information about the spatial distribution of the luminescence. We used a Zeiss Tessar 105 mm focal length f/3.5 camera lens to obtain high-quality images, with the f-stop fully open for maximum sensitivity. A $2.9\times$ magnified image of the crystal was translated in the image plane using a 90° deflection mirror precisely controlled by stepper motors.[36] A luminescence profile obtained by scanning the image across a slit mounted either vertically or horizontally is called a slit scan. A corresponding profile obtained with both horizontal and vertical slits in place is called a box scan.

Slit and box scans were measured for three orthogonal spatial directions, using the mirrors in Fig. 2 to obtain different views of the sample. The views and the conventions for labeling crystal coordinates are shown in Fig. 3. The image was translated by one step of the stepper motor by a distance corresponding to ~ 8 or ~ 12 μm in the crystal for a vertical or horizontal scan, respectively.

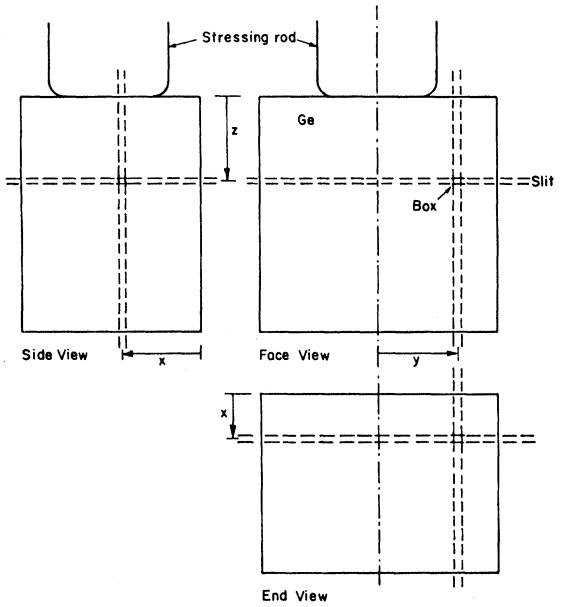

FIG. 3. Definition of the coordinate system used in this paper. For a z scan, either the face or the side view is scanned vertically across a slit or box aperture. For a y scan, either the face or the end view is scanned horizontally across the aperture. For an x scan, the end view is scanned vertically or the side view is scanned horizontally. Zero points for x, y, and z are as shown. The face view is obtained directly while the end and side views use the 45° mirrors shown in Fig. 2.

The spatial resolution depended on several factors, including the resolution of the lens, the focusing accuracy, the aperture size, the sweep speed and time constant, and the optical quality of the crystal surface. We estimated the overall resolution empirically from a series of slit scans recorded for the x, y, and z directions. The drop volume may be computed from the radii R_x, R_y, and R_z, which are given for constant density by[11]

$$R = W_s/\sqrt{2}\,, \tag{1}$$

where W_s is the full width at half-maximum (FWHM) of a slit scan. The volume is shown later in the paper as a function of excitation level (see Fig. 8). The break in the slope for small drop sizes indicates some loss of spatial resolution. We conclude that W_s is a good indicator of drop size for $W_s \gtrsim 100$ μm or $R \gtrsim 70$ μm.

We note that the excitation level is given, as previously,[11] by the actual laser power $P_{\rm abs}$ absorbed into the sample. At the highest excitation levels ($P_{\rm abs} \approx 0.85$ W) sample heating must be considered. A crude estimate of the EHL temperature can be made from the high-energy tail of a luminescence spectrum.[35] We estimate that the EHL temperature may be slightly higher than that of the liquid-helium bath (~ 1.9 K) but is certainly less than 4 K.

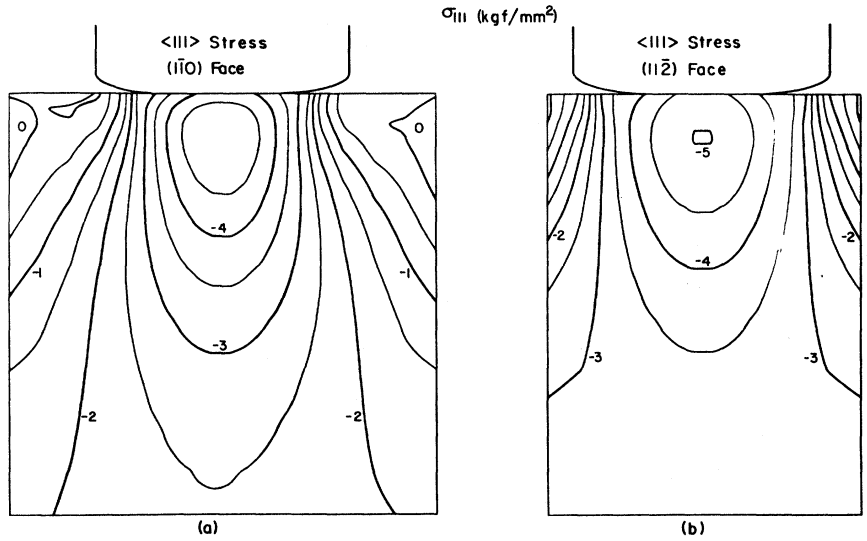

FIG. 4. Two-dimensional calculations of σ_{111}, the $\langle 111 \rangle$ component of stress, with parameters chosen to reproduce experimental conditions in a Ge crystal. (a) Corresponds to face view of sample. (b) Corresponds to side view of sample.

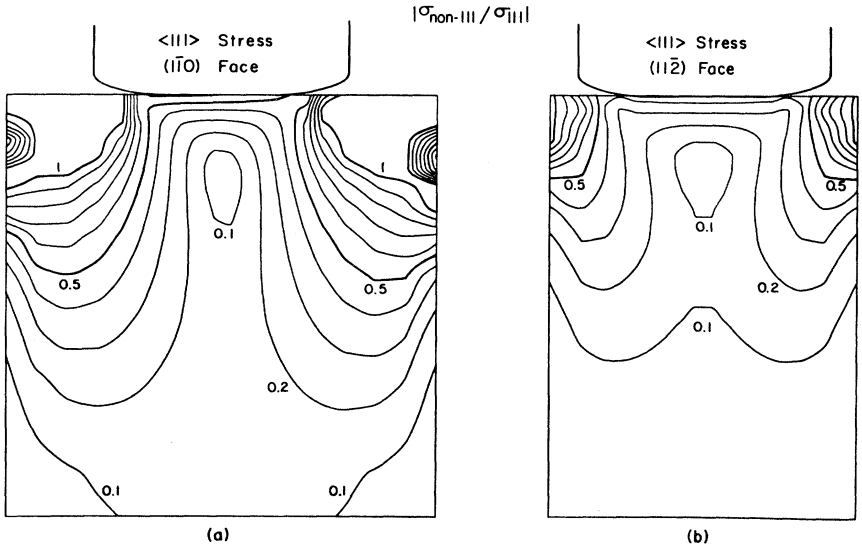

FIG. 5. Two-dimensional calculations of the deviation from uniaxial ⟨111⟩ stress, $\sigma_{\text{non-111}}/\sigma_{111}$. (a) Face view. (b) Side view.

III. CHARACTERIZATION OF THE STRAIN WELL

In order to quantitatively understand the variation of the electron-hole—pair density with position in the SCEHL, it is necessary to characterize the strain well. In this section we discuss the degree to which the stress is uniaxial, the maximum stress σ_m at the center of the well, the equilibrium density n_0, and the shape of the strain well, for both excitons and the EHL.

Our stressing geometry results in a highly nonuniform distribution of stress. The shear strain components and other quantities can be calculated for such a geometry.[5,37] Information about the three-dimensional distribution is inferred from a pair of two-dimensional plots passing through the center of the crystal for perpendicular orientations. Figure 4 shows the results of such a calculation of σ_{111}, the component of stress along the ⟨111⟩ direction, in a Ge crystal. Part (a) represents a slice parallel to a 4×4 mm^2 (1$\bar{1}$0) face, while part (b) represents a slice parallel to a 4×3 mm^2 (11$\bar{2}$) face. Parameters were chosen to approximately reproduce two experimental features: the maximum stress $-\sigma_m\approx5$ kgf/mm^2 (see below) and the position $z_0=0.8$ mm of the well relative to the face touched by the plunger. Note that compressional stresses are negative and that 1 kgf=1 kg force=9.80665 newtons.

The computer program also evaluates other stress components. A measure of the deviation from uniaxial stress is given approximately[38] by the ratio

$$\sigma_{\text{non-111}}/\sigma_{111}=-\sqrt{\sigma_{yy}^2+2\sigma_{yz}^2}/\sigma_{zz}\ , \tag{2}$$

where z is along ⟨111⟩ and $y\perp z$. This quantity is shown in Fig. 5 for the geometry and parameters of Fig. 4. Even for the largest drops studied, $\sigma_{\text{non-111}}/\sigma_{111}\lesssim0.3$. Thus we shall assume uniaxial ⟨111⟩ stress throughout the region of the crystal occupied by the SCEHL.

The maximum stress σ_m at the center of the well cannot be obtained directly from the applied

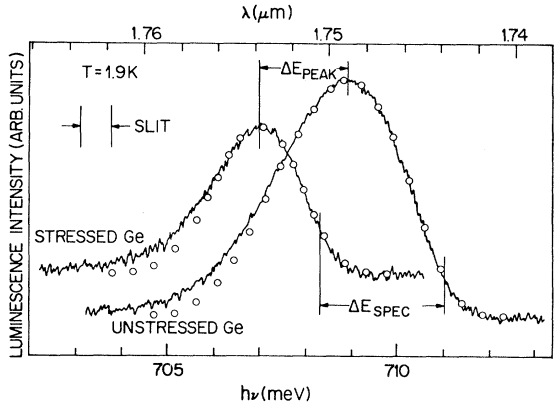

FIG. 6. Luminescence spectra from stressed and unstressed Ge samples for $T=1.9$ K. The open circles give the theoretical line shapes for the best fit. The shifts of the peak energy ΔE_{peak} and of the spectroscopic energy ΔE_{spec} are indicated, along with the spectral resolution.

force and the plunger-sample contact area. We used two methods to estimate σ_m. Figure 6 shows a luminescence spectrum from the stressed sample for low excitation ($P_{abs}=0.8$ mW) and one from unstressed Ge for $P_{abs}=25$ mW. In the first method, the stress is obtained from the shift of the peak energy by comparison with the uniaxial stress data of Benoît à la Guillaume *et al.*,[39] which are fitted by the following expression:

$$\Delta E_{peak}=1.62+0.68\sigma, \quad 2.5\lesssim -\sigma \lesssim 13 , \tag{3}$$

where σ is in kgf/mm^2 and ΔE_{peak} is in meV. From our observed value $\Delta E_{peak}=-1.93$ meV, we find $-\sigma_m=5.2$ kgf/mm^2.

In the second method the stress is obtained from the shift of the Fermi energy, in turn obtained from a line-shape fit. The data of Ref. 39 were not analyzed in sufficient detail to yield these spectroscopic energies, E_{spec}. However,

$$\Delta E_{spec}=\Delta E_{gap}-\Delta f_G , \tag{4}$$

where ΔE_{gap} is the change in the minimum band gap and f_G is the ground-state pair energy with respect to the lowest conduction-band minimum. Using experimental deformation potentials[40] and our calculations[41] of f_G, we find

$$\Delta E_{spec}=1.81+0.77\sigma, \quad 2.5\lesssim -\sigma \lesssim 9 \tag{5}$$

with the same units as for Eq. (3). We obtained the spectroscopic energies shown in Fig. 6 from line-shape fits[42] and found $\Delta E_{spec}=-2.67$ meV, yielding $-\sigma_m=5.8$ kgf/mm^2. The good agreement between the two methods indicates that the change in f_G with stress is described well by the calculations.[41] We show in Sec. V B that the theory of the present paper is not sensitive to small changes in σ_m, so we will present theoretical results for $-\sigma_m=5$ kgf/mm^2.

The line-shape fits also yielded electron-hole–pair densities. For unstressed Ge we used the standard line-shape formula[43] and found $n=2.20\pm0.05\times10^{17}$ cm^{-3}, in good agreement with other published values.[43] For the stressed sample, we used an appropriate modification of the standard formula, including the stress-induced conduction- and valence-band splittings and energy-dependent hole density-of-states masses.[42] The best fit was obtained for

$$n=0.47\pm0.03\times10^{17}\ \text{cm}^{-3} , \quad -\sigma_m=5\ \text{kgf/mm}^2, \quad T=1.9\ \text{K} . \tag{6}$$

Since the spectrum was measured at low excitation, the deduced density is the equilibrium density for this stress. In the figure the open circles give the theoretical line shapes, in which both the spectrometer resolution (0.66 meV FWHM) and the wavelength-dependent detector response are included.

The shape of the strain well can be characterized by the shape of a spatial slit scan of the luminescence emitted by excitons at high temperature in the absence of liquid. If the exciton energy is a parabolic function of the distance r from the center of the well and if the excitons behave like an ideal gas, then the intensity in a slit scan is given by[11]

$$I(x)=I(x_0)\exp[-\alpha_{ex}(x-x_0)^2/kT] , \tag{7}$$

where $x=x_0$ is the center of the well. This form has been observed for strain wells both in ⟨111⟩-stressed Ge (Ref. 11) and in ⟨100⟩-stressed Si.[44] For the present sample, we find that the strain well is accurately parabolic with well parameters $\alpha_{ex}^x=1.9\pm0.1$ meV/mm^2 and $\alpha_{ex}^y=2.0\pm0.2$ meV/mm^2 for the x and y directions.[35] While the upper half of the z scan (above the center of the well) is reasonably parabolic, with $\alpha_{ex}^z=5.5\pm0.5$ meV/mm^2, the lower half is less so, but with an average ~2 meV/mm^2.[35] The latter deviation from parabolicity, as well as the good agreement for the other directions, may be anticipated from the calculations of Fig. 4. A good starting point for the description of the strain well in this sample is a hemisphere plus a hemi-ellipse.

In the stress range of interest (2.5–6 kgf/mm^2), we showed above that E_{spec} and E_{gap} have slightly different stress dependences. The ratio of these stress dependences gives the EHL spectroscopic well parameter, $\alpha_{spec}=0.89\alpha_{ex}$, so that

$$\alpha_{spec}=1.7\pm0.2\ \text{meV/mm}^2 \tag{8}$$

for the x and y directions.

Finally, it is useful to estimate the variation in stress over the volume of the largest drop obtained, $R\approx700$ μm. Using Eqs. (5) and (8) we find that the maximum variation in stress is ~1.1 kgf/mm^2.

IV. QUALITATIVE EVIDENCE FOR COMPRESSION OF THE SCEHL

In a previous study[11] of the properties of the SCEHL, we found that the luminescence spectral linewidth depended on the excitation level. In particular, the linewidth was constant at low excita-

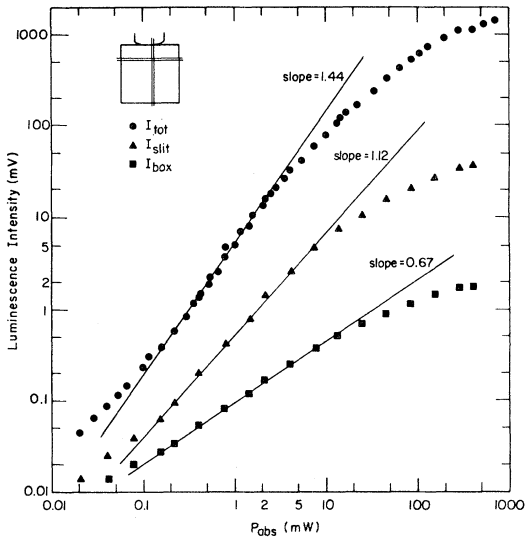

FIG. 7. Total luminescence intensity I_{tot}, peak intensity in a slit scan I_{slit}, and peak intensity in a box scan I_{box}, as a function of absorbed laser power P_{abs}. The inset shows the schematic arrangement for slit and box scans. Slopes are indicated for the same range of excitation levels. The experiment was performed at $T=1.9$ K.

tion but increased substantially at higher excitation levels. In contrast, for unstressed Ge the linewidth is always found to be independent of the excitation level: Indeed, the constant linewidth provides strong support for the identification of a liquid phase. The increase in the luminescence linewidth of the strain-confined EHL at high excitation can have two contributions.[11,31] One is due to the variation of the stress with position in the well: The luminescence is shifted to higher energies near the surface of the drop, where the magnitude of the stress is lower. In addition, an increase in linewidth could indicate an increase in the average electron-hole—pair density.

In the earlier study[11] the initial luminescence decay time τ_i was also studied as a function of excitation level. We found that τ_i was constant at low excitation but decreased, again substantially, at higher excitation levels. Since the recombination processes are generally assumed to depend on stress only through the electron-hole—pair density, and since the contributions to the lifetime depend inversely on the density, the observed decrease in τ_i indicates an increase in the density at high excitation.

Additional qualitative information can be obtained from the excitation dependence of spatial luminescence profiles. Figure 7 shows the peak luminescence intensity for box and slit apertures, I_{box} and I_{slit}, and the total luminescence intensity without spatial selection, I_{tot}, as a function of absorbed laser power, P_{abs}. Figure 8 shows the drop size and volume as a function of P_{abs}, where the drop size is given by W_s and the volume is obtained from the radii and Eq. (1). To aid in the interpretation of these data, straight lines indicate the trends for $0.1 \lesssim P_{abs} \lesssim 5$ mW.

We shall attempt to interpret the data using geometrical arguments for spherical constant-density drops. The total luminescence intensity is a measure of the amount of liquid present. The slope found for I_{tot} in Fig. 7, 1.44, indicates that the production efficiency falls off at low excitation levels, due to the relatively large distance to the strain well from the excited face of the crystal. Geometrically, I_{tot} is a measure of the drop volume and thus should vary with power as R^3, where R is the drop radius. I_{slit} represents a slice through the center of the sphere and should vary as R^2. Similarly, I_{box} represents a core section through the center of the sphere and should vary as R.

It is clear from the slopes given in the figures that these simple relationships are not true. First, the two measures of the drop size, I_{box} and W_s, have very different power dependences, with slopes 0.67 and 0.41, respectively. Second, the two measures of the drop volume, I_{tot} and V, also have different power dependences, with slopes 1.44 and 1.24, respectively. Third, the slopes for I_{box}, I_{slit}, and I_{tot} have the relation 0.67:1.12:1.44, which does not correspond to the expected relation $a:2a:3a$ ($a \neq 1$ indicates varying production effi-

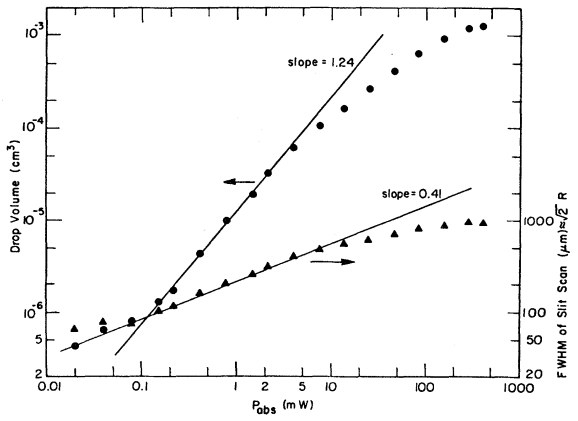

FIG. 8. Drop size and volume vs absorbed power. The slopes are indicated for the same range of excitation levels as for Fig. 7. $T=1.9$ K.

ciency). All these deviations from the simple geometrical model can be understood qualitatively if the density varies with position within the drop, if the density is higher at the center of the drop, and if the density at the center of the drop increases with drop size.

V. THEORY OF THE DENSITY VARIATION

In this section we show theoretically how a density variation such as the one described qualitatively in the preceding section can occur. We describe a first-order theory in order to gain some physical insight. Then we present a more exact theory.

A. First-order theory

The basis for a variation of density with position in the SCEHL consists of two facts: (1) the pair energy varies with density in the EHL, and (2) the SCEHL sits in a potential energy well, so that the energy varies with position in the drop. In the absence of a strain well, the equilibrium density $n_0(T)$ (for low T) is that for which the pair energy is a minimum. The liquid can have a density other than $n_0(T)$ only at the cost of an increase in energy. In the strain well, for small drop sizes the change in energy across the drop is small, and the density is nearly uniform with the equilibrium value. As the drop grows larger it occupies regions of higher strain energy and the average pair energy is forced to increase. However, the *total* drop energy can be reduced if the liquid becomes more dense at the center, where the strain energy is lower. Thus, the density will vary with position with densities higher than $n_0(T)$ in the interior of the drop.

The condition which determines the form of the density distribution is that the chemical potential is a constant throughout the drop volume. This means that the liquid is in diffusive equilibrium: The time required for particles to travel across the drop is much less than the drop lifetime. We verify this condition by estimating a carrier Fermi velocity

$$v_F=\sqrt{2E_F/m}\approx 4\times 10^6 \text{ cm/sec} , \tag{9}$$

where we have used $E_F\approx 2$ meV and $m\approx 0.4m_0$ to underestimate v_F. The greatest distance to be traveled is the diameter of the largest drop studied, ~ 1.4 mm, so that the maximum transit time is less than ~ 0.035 μsec, much less than the drop lifetime $\tau\approx 500$ μsec. Thus the assumption of constant chemical potential is certainly justified.

We review the first-order theory which has been outlined previously[31] for $T=0$. The pair free energy is expanded about the minimum:

$$E=E_0+\tfrac{1}{2}E_0''(n-n_0)^2+E_s(r) , \tag{10a}$$

where n_0 and E_0 are the ground-state density and energy, $E_0''=d^2E/dn^2\,|_{n_0}$, and the strain energy is assumed to be parabolic in the distance r from the center of the well:

$$E_s(r)=\alpha_{\text{spec}}r^2 . \tag{10b}$$

The pressure is given by

$$P=n^2\frac{dE}{dn}=n^2E_0''(n-n_0) . \tag{11}$$

To first order in $n-n_0$ the chemical potential can be written

$$\mu=E+n\frac{dE}{dn}$$

$$=E_0+n_0E_0''(n-n_0)+\alpha_{\text{spec}}r^2=\text{const} . \tag{12}$$

An expression for the density as a function of position, $n(r)$, can be obtained using Eq. (12) for arbitrary r and for $r=R$:

$$n(r)=n(R)[1+\beta(R)(1-r^2/R^2)] , \tag{13a}$$

where

$$\beta(R)=\alpha_{\text{spec}}R^2/[n(R)n_0E_0''] . \tag{13b}$$

Thus the density profile is parabolic, increasing from $n(R)$ at the surface to

$$n(0)=n(R)[1+\beta(R)] \tag{13c}$$

at the center of the drop.

The density at the surface of the drop is obtained as follows. We note that the change in pressure across the drop surface is given by[45]

$$P_{\text{liquid}}-P_{\text{gas}}=S/R , \tag{14}$$

where $S\approx 1\times 10^{-4}$ erg/cm^2 is the surface tension.[46] Even for the smallest drops studied here, $R\approx 50$ μm, the pressure difference ~ 0.02 dyn/cm^2 corresponds to a negligible correction to the liquid density. Thus

$$n(R)=n_0 . \tag{15}$$

Actually, since the equilibrium density varies with stress,[31,41] $n(R)$ depends on the drop size. However, this change is relatively small: Our calculated equilibrium density changes by only about 10%

over the included stress range for our largest drops (~ 1.1 kgf/mm^2). This small change in n_0 with drop size will be neglected, since it is much smaller than the density variation implied by Eq. (13). The central density can be estimated using $n_0^2 E_0''$ $=0.42$ meV (Ref. 47) and $\alpha_{\rm spec}=1.7$ meV/mm^2. The density variation is less than 10% if $R<160$ μm, while for $R=700$ μm we predict $n(0)\approx 3.0 n_0$.

The magnitude of the density variation for large drop sizes may at first be surprising, since most liquids are not very compressible. If a hard-sphere model is used to describe the liquid atoms or molecules, the interparticle spacing in most liquids is close to the size of the sphere. However, in the electron-hole liquid the wave functions of the constituent particles can have considerable overlap. The equilibrium interparticle spacing is approximately the exciton Bohr radius, but the hard-sphere radius would be much smaller. Thus the compressibility of the EHL can be much greater than that of ordinary liquids.

It is clear that Eq. (13) is no longer valid for large drop sizes, since the deviations from n_0 are no longer small. Hence a more exact theoretical treatment is necessary. Before turning to that, however, it is useful to estimate within the first-order theory the effect of temperature on the density profile. For example, in studying the electron-hole liquid-gas phase diagram in a strain well, we shall see that for elevated temperature it is necessary to account for the compression of the liquid even for relatively small drop sizes. For finite T the pair energy of Eq. (10a) becomes:

$$E=E_0(T)+\tfrac{1}{2}E_0''(T)[n-n_0(T)]^2+\alpha_{\rm spec}r^2 . \quad (16)$$

In Eq. (13), $n(R)=n_0(T)$ and $\beta(R,T)$ now depend on T. For simplicity we consider a low-T expansion

$$E=E_0+\tfrac{1}{2}E_0''(n-n_0)^2-\tfrac{1}{2}\gamma(n)T^2+\alpha_{\rm spec}r^2 , \quad (17)$$

and assume[48] that $\gamma(n)\sim n^{-2/3}$. Then we find

$$\beta(R,T)=\beta(R,0)[1+\tfrac{11}{3}\delta_n(kT)^2] , \quad (18a)$$

where δ_n is defined by

$$n_0(T)=n_0[1-\delta_n(kT)^2] . \quad (18b)$$

We can use Eq. (18a) to estimate the largest drop size for which the density is uniform to within 10% at $T=4.2$ K. Using $\delta_n=3.8$ meV^{-2} (Ref. 47) and the values given above, we find $R\approx 95$ μm. For a steeper strain well, the requirement is more stringent: Using a typical value[11] $\alpha_{\rm spec}=8$ meV/mm^2 we find $R\approx 45$ μm. At high temperatures, then, the liquid may already be appreciably compressed at the smallest drop sizes for which enough luminescence can be collected for an accurate line-shape fit.

It is interesting to consider the temperature dependence of the central density:

$$n(0,T)=n_0[1+\beta(R,0)] +n_0[8\beta(R,0)/3-1]\delta_n(kT)^2 . \quad (19)$$

The sign of the temperature coefficient depends on the drop size through $\beta(R,0)$. For small radii, the coefficient is negative and the liquid expands as the temperature rises. For larger drops, however, the compression is more important and $n(0,T)$ actually increases with T. For $\alpha_{\rm spec}=1.7$ meV/mm^2 the temperature coefficient changes sign at $R\approx 300$ μm.

Since many experiments measure an average density, it is useful to have an expression for it. Using the form of Eq. (13a) we have

$$\bar{n}\equiv\frac{1}{V}\int n(r)dV=n_0(1+2\beta/5) . \quad (20)$$

For finite temperature an expression analogous to Eq. (18b) may be obtained:

$$\bar{n}(T)=\bar{n}(0)[1-\delta_n^{\rm eff}(kT)^2] , \quad (21a)$$

where

$$\delta_n^{\rm eff}=\frac{1-16\beta(R,0)/15}{1+2\beta(R,0)/5}\delta_n . \quad (21b)$$

Using $n_0^2E_0''=0.42$ meV, $R=150$ μm, and $\alpha_{\rm spec}=1.7$ meV/mm^2, we find $\delta_n^{\rm eff}/\delta_n=0.87$. However, for $\alpha_{\rm spec}=8$ meV/mm^2 the ratio becomes 0.46. If the density variation is not taken into account, substantial errors can occur in the measurement of quantities such as δ_n and the compressibility (see Sec. VIII).

B. Exact theory

The preceding section was intended to give some physical insight into the variation of the density with position in the SCEHL. The numerical examples must in some cases be taken only as guidelines, however, since the first-order theory is not valid for large deviations from n_0. For quantitative analysis a more exact theory must be used:

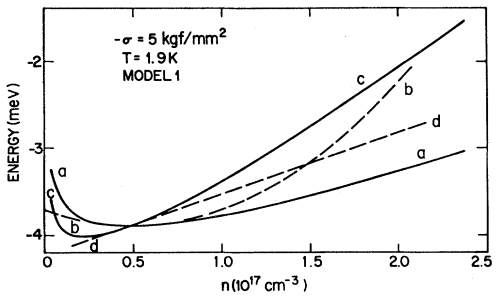

FIG. 9. Electron-hole—pair free energy and chemical potential vs density for $-\sigma=5$ kgf/mm^2 and $T=1.9$ K. *a*, Free energy, model 1. *b*, Free energy, first-order theory. *c*, Chemical potential, model 1. *d*, Chemical potential, first-order theory.

Equation (10a) must be replaced by a full calculation of the pair free energy as a function of density. Such a calculation has been described for finite stress and temperature[41]: Here we will use our results for model 1. Figure 9 illustrates the differences between the full model-1 calculation (solid curves) and the first-order calculation (dashed curves) of the free energy (curves *a* and *b*) and the chemical potential (curves *c* and *d*) for $-\sigma=5$ kgf/mm^2 and $T=1.9$ K, omitting the strain energy term. It is clear that the full calculation must be used when the density deviates significantly from n_0.

We assumed implicitly in the discussion of the first-order theory that the effect of the strain well is contained entirely in the term $E_s(r)$, i.e., that the density dependence of the free energy is independent of drop size and hence of stress. This is verified explicitly in Fig. 10, where we show curves for $\mu(n)$ for $-\sigma=3$ and 5 kgf/mm^2, shifted vertically to coincide at approximately the equilibrium density. The difference between these two stresses is nearly twice the range included in the largest drops studied. Except for an additive constant, the curves are very similar over a wide range of densities. With the information given previously, we conclude that the strain well may be adequately described by a uniaxial stress σ_m and a strain energy term $E_s(r)=\alpha_{\rm spec}r^2$.

It will be convenient to express some energies relative to the valence-band maximum; such energies will be labeled with an asterisk. Thus

$$f^*(n,T,\sigma_m,r)=E_{\rm gap}(\sigma_m)+f(n,T,\sigma_m)+\alpha_{\rm spec}r^2\,, \tag{22a}$$

$$P(n,T,\sigma_m,r)=n^2\frac{\partial f^*(n,T,\sigma_m,r)}{\partial n}=n^2\frac{\partial f(n,T,\sigma_m)}{\partial n}\,, \tag{22b}$$

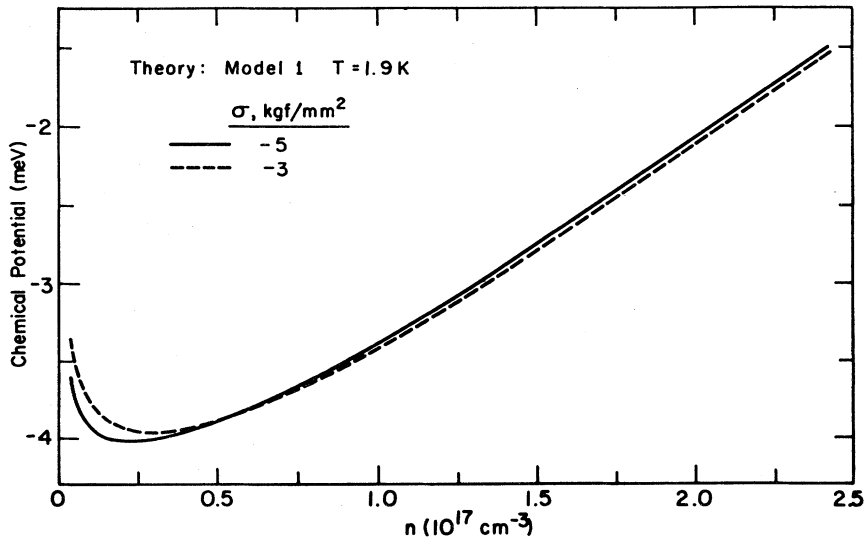

FIG. 10. Chemical potential vs density for two values of stress. The curve for $-\sigma=3$ kgf/mm^2 has been shifted vertically to coincide with the curve for $-\sigma=5$ kgf/mm^2 at approximately the equilibrium density.

TABLE I. Coefficients for density power series.

Coefficient	Value	Unit
$n_0(T)$	0.493	10^{17} cm^{-3}
A_1	1.391	10^{17} cm^{-3}meV^{-1}
A_2	−1.703	10^{17} cm^{-3}meV^{-2}
A_3	3.413	10^{17} cm^{-3}meV^{-3}
A_4	−4.524	10^{17} cm^{-3}meV^{-4}
A_5	3.651	10^{17} cm^{-3}meV^{-5}
A_6	−1.725	10^{17} cm^{-3}meV^{-6}
A_7	0.491	10^{17} cm^{-3}meV^{-7}
A_8	−0.125	10^{17} cm^{-3}meV^{-8}
A_9	0.0401	10^{17} cm^{-3}meV^{-9}
A_{10}	−0.0070	10^{17} cm^{-3}meV^{-10}

$$\mu^*(n,T,\sigma_m,r)=E_{\rm gap}(\sigma_m)+\mu(n,T,\sigma_m)+\alpha_{\rm spec}r^2\ , \tag{22c}$$

where $E_{\rm gap}(\sigma_m)$ is the minimum valence-conduction band gap for the stress σ_m, and f and μ are the model-1 calculations measured as usual with respect to the conduction band. The chemical potential for a drop with radius R is given by

$$\mu_R^*=E_{\rm gap}(\sigma_m)+\mu(n_0(T),T,\sigma_m)+\alpha_{\rm spec}R^2 =\mu_0^*+\alpha_{\rm spec}R^2\ , \tag{23}$$

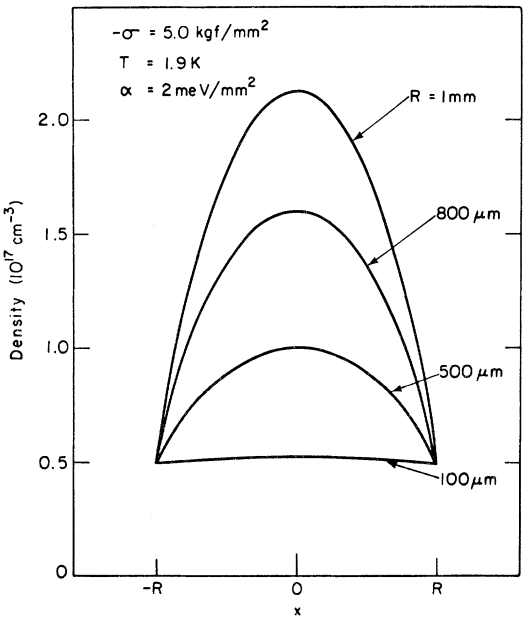

FIG. 11. Theoretical density profiles for different drop sizes calculated using Eq. (25) for $-\sigma=5$ kgf/mm^2, $T=1.9$ K, and $\alpha_{\rm spec}=2$ meV/mm^2. The position variable x is normalized to the drop radius R.

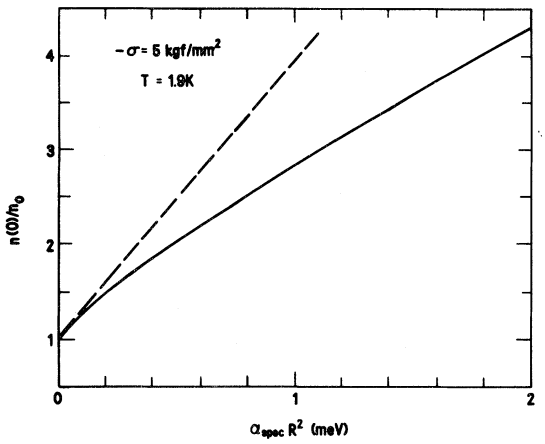

FIG. 12. Calculated normalized central density vs $\alpha_{\rm spec}R^2$, for $-\sigma=5$ kgf/mm^2 and $T=1.9$ K. The solid curve is the exact theory and the dashed line is the first-order calculation.

where μ_0^* is the chemical potential in the limit of zero drop size. This quadratic dependence of μ_0^* on drop size holds as long as the strain well is parabolic.

As for the first-order theory, Eqs. (22c) and (23) may be combined for arbitrary r and for $r=R$:

$$\mu(n(r,R,T),T,\sigma_m)-\mu(n_0(T),T,\sigma_m)=\alpha_{\rm spec}(R^2-r^2)\ . \tag{24}$$

This implicit equation must be solved for the density profile $n(r,R,T)$. It is convenient to express the density difference $n(r,R,T)-n_0(T)$ as a power series in the chemical potential difference $\mu(n)-\mu(n_0)$ (Ref. 49) so that

$$n(r,R,T)=n_0(T)+\sum_{i=1}^{10}A_i[\alpha_{\rm spec}(R^2-r^2)]^i\ . \tag{25}$$

We included chemical potential differences up to 2 meV and used ten terms in our fit. Values for $n_0(T)$ and the A_i are listed in Table I for $-\sigma=5$ kgf/mm^2 and $T=1.9$ K.

Several density profiles calculated according to Eq. (25) are shown in Fig. 11 for $\alpha_{\rm spec}=2$ meV/mm^2, where the position variable x is normalized to the drop radius. These profiles appear qualitatively to be parabolic. We have shown[35] that they are indeed very nearly parabolic, with parameters determined by the central densities of Eq. (25) and by Eq. (15). Thus we may write

$$n(r,R,T)=n_0(T)[1+\beta(R,T)(1-r^2/R^2)]\ , \tag{26a}$$

where

$$\beta(R,T)=\sum_{i=1}^{10} A_i(\alpha_{\text{spec}}R^2)^i/n_0(T) \ . \tag{26b}$$

The calculation of luminescence profiles (see Sec. VI) is simplified by using this formula.

We note that $\beta(R,T)$ is not simply proportional to R^2, as it was in Eq. (13). We illustrate the difference in Fig. 12, where we show the normalized central density $n(0)/n_0=1+\beta$ as a function of $\alpha_{\text{spec}}R^2$. The solid curve is the exact theory of Eq. (26b), while the dashed line is the corresponding first-order theory using $n_0^2(T)E_0''(T)=0.34$ meV. For $\alpha_{\text{spec}}=1.7$ meV/mm^2 we find, as previously, that the density variation will be less than 10% if $R<160$ μm. For $R=700$ μm, the exact theory yields $n(0)\approx 2.6n_0$ while the first-order result has increased to $n(0)\approx 3.4n_0$ because of the decrease in $n_0^2E_0''$ at finite T. The first-order theory overestimates the density increase for large drop sizes, but the variation is still quite substantial.

The results of Fig. 12 can easily be used for other strain well conditions. For example, $\alpha_{\text{spec}}R^2=1$ meV corresponds to $\alpha_{\text{spec}}=2$ meV/mm^2 and $R=707$ μm or to $\alpha_{\text{spec}}=8$ meV/mm^2 and $R=354$ μm. In addition, since the chemical potential versus density does not change too rapidly with stress (see Fig. 10), the calculation will be fairly accurate for a range of stresses, at comparable temperatures.

We conclude this section with a determination of the maximum drop size and central density for a given stress σ_m. We note that for stresses smaller (in magnitude) than $\sigma_{\min}\approx -2.6$ kgf/mm^2, the ground-state energy μ_0^*, measured from the valence band, does not decrease with stress.[50] Therefore, it is not energetically favorable for the EHL to be in a region of the crystal where $|\sigma|<|\sigma_{\min}|$. Hence the chemical potential $\mu_R^*(\sigma_m)$ for a drop of radius R and stress σ_m cannot exceed the value $\mu_0^*(\sigma_{\min})$. The maximum drop radius $R_{\max}$ is given by

$$\alpha_{\text{spec}}R_{\max}^2=\mu_0^*(\sigma_{\min})-\mu_0^*(\sigma_m) \ . \tag{27}$$

For $-\sigma_m=5$ kgf/mm^2, we find $\alpha_{\text{spec}}R_{\max}^2=1.8$ meV. In the experiment, our maximum value of $\alpha_{\text{spec}}R^2$ was ~ 0.85 meV, so the well was only about halfway full. Because the drop radius is limited, the density $n(0,R_{\max},T)$ is also limited. For the same conditions as above, the maximum density is $\sim 2.2\times 10^{17}$ cm^{-3}. Thus a range of densities is accessible simply by changing the excitation level to change the drop size. The available range increases with σ_m, with a maximum density of $\sim 4.5\times 10^{17}$ cm^{-3} for $-\sigma_m=10$ kgf/mm^2.

VI. MANIFESTATION OF THE DENSITY VARIATION IN SPATIAL LUMINESCENCE PROFILES

Because the density variations predicted in the last section can be so large, many types of luminescence experiments are affected. In this section we shall investigate the effects on spatial luminescence profiles and describe a method to measure the density variations directly. The radiative decay rate for pairs in a small volume dV located at a position r is

$$dI(r)=\frac{n(r)}{\tau_{\text{rad}}(n)}dV \ , \tag{28}$$

which may be integrated over V to give the radiated power. The radiative lifetime is given by

$$\tau_{\text{rad}}^{-1}(n)=B_0\rho(n)n \ . \tag{29}$$

Here B_0 is a constant which is proportional to $|D|^2|H|^2/|\delta E|^2$, where D is the optical matrix element, H is the electron-phonon matrix element, and δE is an energy difference.[39,51] For simplicity B_0 is assumed to be independent of parameters such as stress and magnetic field; its stress and field dependences are unknown but hopefully small.[52] The enhancement factor $\rho(n)$ is the ratio of the probability of finding an electron and a hole at zero separation in the EHL to the same probability for uncorrelated carriers. At high densities ρ approaches 1 as screening causes the carriers to lose their correlation. At low densities the carriers can become more highly correlated and ρ increases, eventually becoming proportional to n^{-1} so that τ_{rad} becomes independent of n. The low-density limit for τ_{rad} should be close to the free-exciton radiative lifetime, which is at least ~ 1.5 msec in stressed Ge.[53,54]

We use the results of Vashishta's fully self-consistent (FSC) calculation of the enhancement factor corresponding to the model-1 correlation energy.[55] Over a limited density range $\rho(n)$ may be represented by

$$\rho(n)=2.86n_{17}^{-0.384}, \quad 0.4\lesssim n_{17}\lesssim 2.5 \tag{30}$$

where n_{17} is the density expressed in units of 10^{17} cm^{-3}. The FSC calculation yields a steeper density dependence for ρ than less sophisticated models.[56]

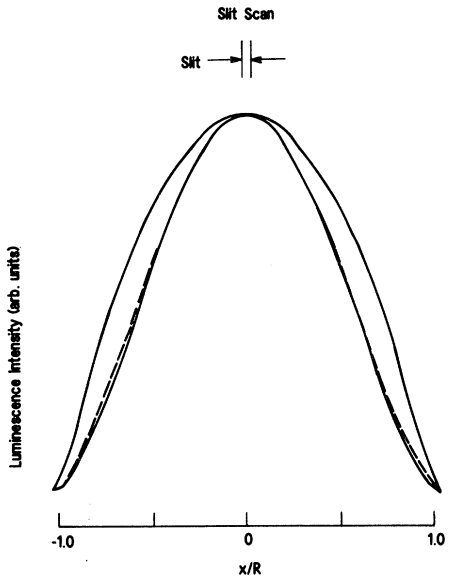

FIG. 13. Theoretical luminescence slit scans from Eq. (31). Outer curve: uniform density. Inner curves: the density distribution of Eq. (26) with $n(0)=2.8n_0$. Dashed curve: includes $\rho(n)$ from Eq. (30). Solid curve: omits $\rho(n)$. The slit width $s=0.05R$.

A slit scan along the x direction in the crystal is given by

$$I_{\text{slit}}(x)=B_0\int_{x-s/2}^{x+s/2}dx\int_{-R}^{R}dy\int_{-R}^{R}dz\,n^2(r)\rho(n)\,, \tag{31}$$

where $x^2+y^2+z^2=r^2$, R is the drop radius, and s is the effective slit width on the sample. Figure 13 shows the effect on a slit scan of the density distribution given in the preceding section. The outer curve shows a slit scan for constant density, for which $I_{\text{slit}}(x)\sim R^2-x^2$ for small slit widths. The inner curves use the density profile of Eq. (26) with $n(0)=2.8n_0$. The dashed curve includes $\rho(n)$ from Eq. (30), while the inner solid curve omits $\rho(n)$. For all three curves $s=0.05R$, so the effect of the finite slit width is small. The effect of $\rho(n)$ on the shape of the profile is negligible. The effect of the density distribution, however, is substantial: The profile is more peaked in the center, and the full width at half-maximum of the profile, W_s, is reduced.

A similar calculation may be performed for a box scan. In this case

$$I_{\text{box}}(x;z=0)=B_0\int_{x-s/2}^{x+s/2}dx\int_{-R}^{R}dy\int_{-s/2}^{s/2}dz\,n^2(r)\rho(n)\,, \tag{32}$$

where the two crossed slits have the same width, s. Figure 14 shows the effect on a box scan of the same density distribution as for Fig. 13. For constant density and a small slit width $I_{\text{box}}(x)\sim(R^2-x^2)^{1/2}$, so that the edge of the drop is very well defined. The effect of the density variation is larger on a box scan than on a slit scan. The full width at half-maximum, W_b, of the inner curves has become almost as narrow as W_s. These qualitative features should be readily observable experimentally, as long as $s\ll R$.

The primary factor which determines the *shape* of a slit or box scan is the density distribution. But this also has a strong effect on the peak *intensity* of the scan. A drop with, e.g., $n(0)=2.8n_0$ contains more electron-hole pairs than a drop with a constant density n_0 and it luminesces more intensely. I_{box} emphasizes the higher-density central region of the drop as compared to I_{slit} or I_{tot}. For this example, the ratio of values for I_{slit} with and without the density distribution is 2.9, while the corresponding ratio for I_{box} is 3.7.

Several features of Figs. 7 and 8 are now clear.

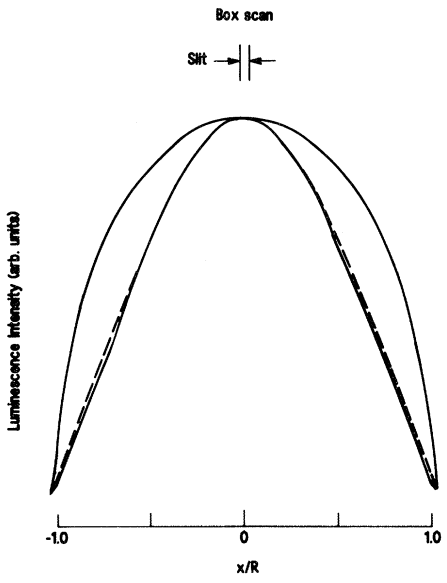

FIG. 14. As Fig. 13, but box scans from Eq. (32).

In the presence of drop-size–dependent density profiles, W_s should increase with excitation more slowly than R, while I_{box} should increase more rapidly than R. Similarly, I_{slit} should increase more rapidly than R^2 or W_s^2 but less rapidly than I_{box}^2. In addition, I_{tot} should increase more rapidly than R^3 or W_s^3 but less rapidly than $I_{slit}^{3/2}$ or I_{box}^3. These relationships indeed are observed in the data.

A more quantitative comparison of peak intensities is obtained by plotting them as a function of drop size W_s rather than excitation level. In Fig. 15 we show I_{tot}, I_{slit}, and I_{box} as a function of W_s for constant density ($n=n_0$) and for the density distribution of Eq. (26) with $\alpha_{spec}=2$ and 8 meV/mm^2. The calculations were performed using an effective slit width $s=35$ μm. For constant density, we find the expected slopes of 1, 2, and 3 for I_{tot}, I_{slit}, and I_{box}, respectively, with small deviations at small drop sizes due to the finite slit width. The deviations from the constant-density case become more pronounced as the strain well becomes steeper and as the drop size increases; they are more pronounced for I_{box} than for I_{slit} and in turn for I_{slit} than for I_{tot}.

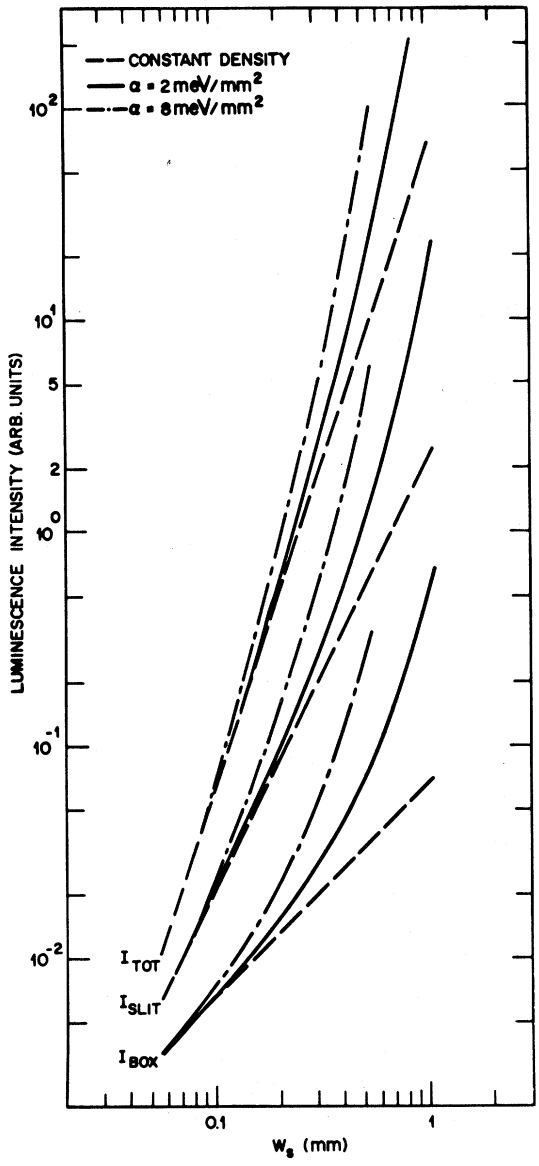

FIG. 15. Calculation of several luminescence intensities as a function of W_s, for constant density and for the density distribution of Eq. (26) with two values for the well parameter α. The slit width was 35 μm.

The density profiles discussed above can be measured directly from luminescence spatial profiles, using Abel transforms. This technique is used in plasma physics and astrophysics to analyze the radial distribution of plasma radiation.[57] The plasma is assumed to be optically thin (no reabsorption of the radiation by the plasma) and to have cylindrical or spherical symmetry. These conditions are applicable for the EHL; we show below that the circular symmetry condition is easily relaxed to elliptical symmetry. This technique has been used to study via the absorption of 3.39-μm light the electron-hole pair density distribution both in the EHD cloud in unstressed Ge[58] and in a relatively small drop of SCEHL in inhomogeneously stressed Ge.[22,59] Many numerical methods are in the literature.[60]

The density distribution is obtained from a luminescence box scan. For the mathematical formalism, we consider infinitely narrow slits. The box scan intensity corresponding to Eq. (32) is

$$\Phi(x)=B_0\int_{-R}^{R} dy\, n^2(r)\rho(n)\ , \tag{33a}$$

where we note that $n(r)=0$ for $r>R$. If the density distribution is circularly symmetric in the x and y dimensions, then

$$\Phi(x)=2B_0\int_x^{\infty}\frac{n^2(w)\rho(n)w\,dw}{\sqrt{w^2-x^2}}\ , \tag{33b}$$

where $w^2=x^2+y^2$ and we assume $z=0$. If the coordinates x and y are related by elliptical symmetry, then $w^2=x^2+ay^2$ with $a=\alpha_y/\alpha_x$, and the right-hand side of Eq. (33b) would be multiplied by $a^{-1/2}$. Now $\Phi(x)$ is simply the Abel transform of the quantity $n^2(w)\rho(n)$. The inverse transform to obtain the density distribution can be written in two ways[61,62]:

$$n^2(w)\rho(n) = -\frac{1}{\pi B_0}\int_w^\infty \frac{\Phi'(x)}{\sqrt{x^2-w^2}}dx \tag{34a}$$

$$= -\frac{1}{\pi B_0 w}\frac{d}{dw}\int_w^\infty \frac{\Phi(x)}{\sqrt{x^2-w^2}}x\,dx\ , \tag{34b}$$

where $\Phi'(x)=d\Phi(x)/dx$. The difference is whether the derivative is taken before or after performing the integration. Although the first method appears to be more common[57,60,61] we use the second[62] here. We did not compare their treatments of experimental noise. A mathematical rearrangement of Eq. (34b) removed apparent singularities in the transform.[35]

Density profiles obtained using Eq. (34) can be directly compared for different experimental conditions. The absolute density scale is determined from a spectral line-shape fit for a small drop, where the density is very nearly uniform. Thus the density scale is as accurate as the line-shape fits, typically plus or minus a few percent. In contrast, we note that density determinations using the absorption of 3.39-μm radiation have a large uncertainty because they rely on an absolute measurement of the hole absorption cross section, which is not accurately known.[21,22,58,63] The absolute accuracy of the density calibration is crucial in obtaining a reasonable value for the compressibility (see Sec. VIII).

VII. EXPERIMENTAL DENSITY PROFILES

An experiment which clearly shows that density variations occur in the SCEHL is the dependence of the peak intensities of slit and box scans on the drop size. Figures 16 and 17 show side and face view data for $I_{\rm tot}$, $I_{\rm slit}$, $I_{\rm box}$, and the peak intensity I_λ in a luminescence spectrum obtained from a slice at the center of the drop. The slit and box scans were both x scans (Fig. 16) and y scans (Fig. 17). The theoretical curves are for $\alpha_{\rm spec}=2$ meV/mm^2 and a slit resolution of 35 μm.[64] The relative intensities of the curves are kept intact. The agreement between experiment and theory is excellent over nearly an order of magnitude variation in drop size. The deviations for small drop size are due to a loss of resolution on a scale larger than the slit width.

The box scans were further analyzed to obtain density profiles. The choice of views and scan directions was deliberate: In a side-view x scan the luminescence is integrated through the y direction, while in a face-view y scan the luminescence is integrated through the x direction. These coordinates are accurately related by elliptical symmetry, so that the Abel transform is mathematically correct. Scans involving z are not analyzed here.

An example of a box scan obtained for $P_{\rm abs}=400$ mW is shown in Fig. 18, while the corresponding density profile is shown in Fig. 19. The extra luminescence at the left side of Fig. 18 comes from small droplets flowing into the strain well from the excitation point at $x-x_0\approx -1.5$ mm. A constant baseline correction and a simple smoothing procedure were applied to the raw data before the transform of Eq. (34). The left and right halves of the box scan were processed separately. The raw data in Fig. 18 show several wiggles, apparently due to small imperfections on the crystal face through which the luminescence image was obtained. These relatively small anomalies are magnified by the transform: Because the box scan is a superposition of luminescence through the depth of the well, a dip (for example) in the box scan intensity corresponds to a much larger dip in the density. The density appears to go smoothly to zero in Fig. 19 because the finite slit width smears out the abrupt change at the surface of the drop ($x-x_0\approx\pm 0.7$ mm). This means that $n(R)$ cannot be measured from such a density profile.

The most important feature of Fig. 19 is that the electron-hole–pair density has large variations with position. The form of the spatial density profile agrees well with our theoretical prediction: The solid curve shows the transform of a theoretical box scan computed using $\alpha_{\rm spec}=2$ meV/mm^2, $R=0.7$ mm, and $s=35$ μm.[65] For comparison, the figure also shows the expected form of the transform if the density were uniform but still compressed from the equilibrium value. The dashed curve represents a "best fit" for a constant density. The essential validity of the theory of Sec. V is thus confirmed.

Figure 20 shows a series of density profiles obtained for $P_{\rm abs}=400$, 7.4, and 0.22 mW. This illustrates the feasibility of measuring density profiles for widely varying excitations and drop sizes. We find that the central density increases by a factor of approximately 3.5 for this range of conditions.[65] For small drop sizes, because of the finite slit width, it is difficult to tell from the transform of a *single* scan whether or not the density varies significantly with position. This may possibly explain the null result of Mattos *et al.*[22,59] Thus, it is important to study density profiles as a function of drop size.

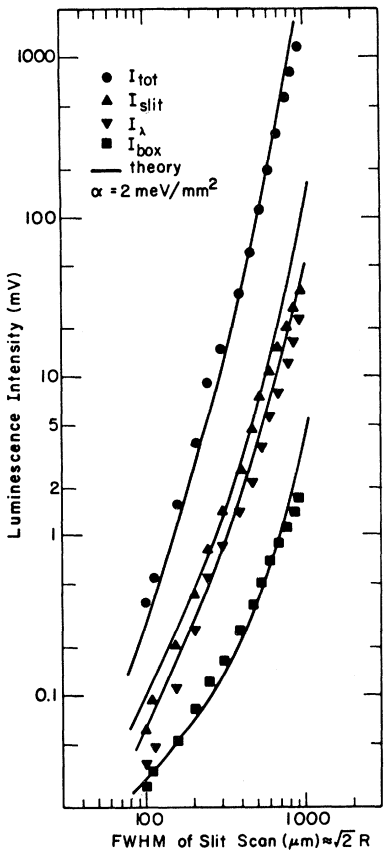

FIG. 16. Luminescence intensities I_{tot}, I_{slit}, I_{box}, and the peak intensity in a spectrum I_{λ} as a function of W_s for x scans obtained from the side view. The theoretical curves are for $\alpha_{spec}=2$ meV/mm^2 and slit resolution 35 μm. $T=1.9$ K.

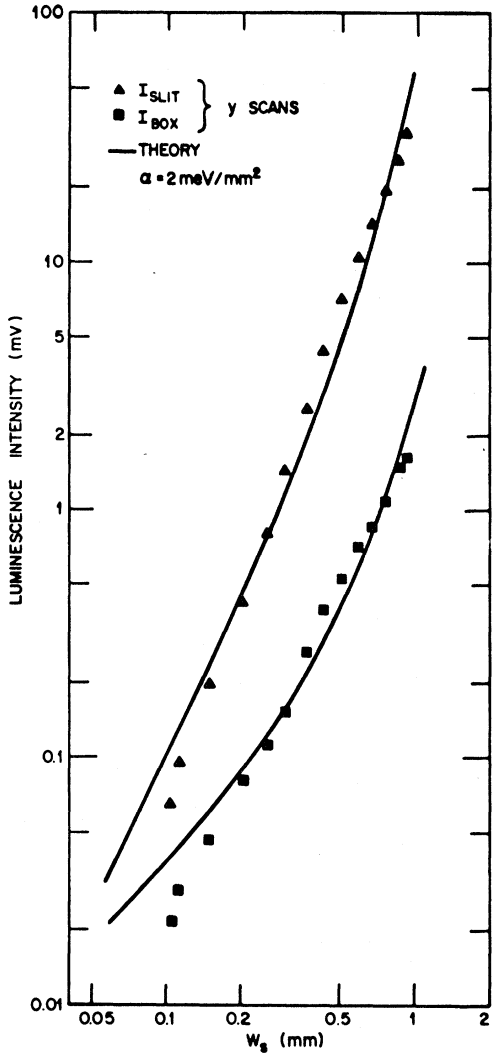

FIG. 17. As Fig. 16, for y scans obtained from the face view.

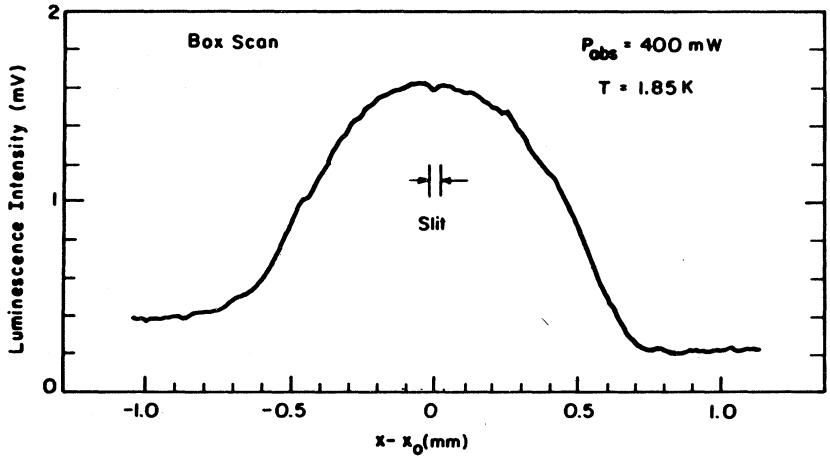

FIG. 18. Box scan obtained by translating the luminescence image of the Ge crystal across a small aperture. $P_{abs}=400$ mW, $T=1.85$ K, slit width ≈ 35 μm.

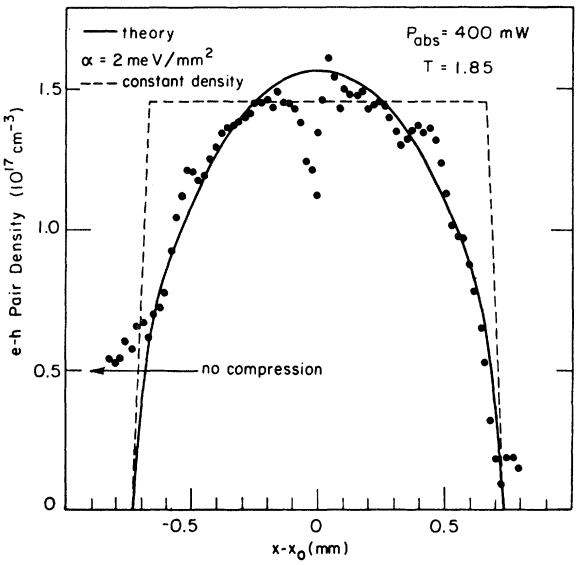

FIG. 19. Electron-hole (e-h) pair density profile obtained by performing an Abel transform of Fig. 18. Solid curve: transform of a theoretical box scan including a slit width $s=35$ μm. Dashed curve: "best fit" for a constant density.

The central densities $n(0)$ for 24 profiles including both x scans and y scans are shown in Fig. 21 as a function of W_s. The theoretical curve was obtained using our measured α_{spec} and normalized to the equilibrium density obtained from the lineshape analysis. The absolute density scale for the data was determined by requiring agreement with the spectral line shape for small drop size. We used the form of $\rho(n)$ given in Eq. (30) in our analysis; we note that using $\rho=$const gives somewhat less variation in $n(0)$. Overall, the agreement between experiment and theory is quite satisfactory. Deviations can result from nonparabolicity of the strain well for large drop sizes.

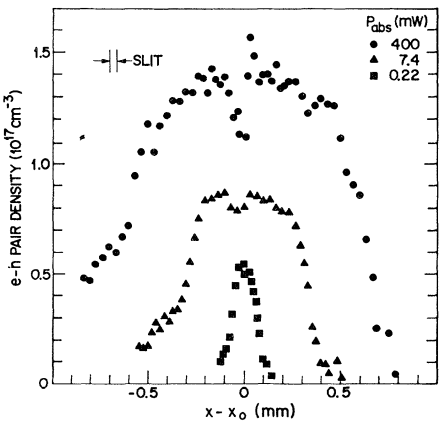

FIG. 20. Density profiles obtained from box scans for a series of excitation levels.

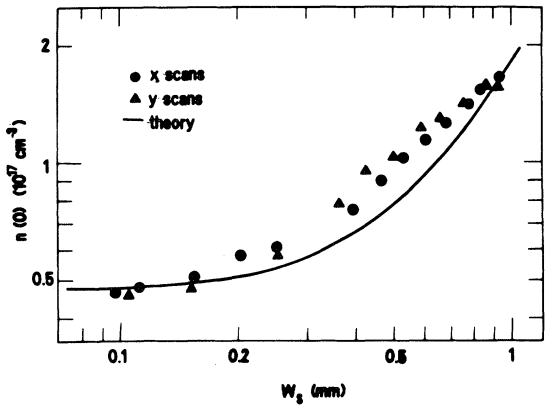

FIG. 21. Central density as a function of drop size for two sets of data. The theoretical curve is for $\alpha_{\text{spec}}=2$ meV/mm^2.

VIII. CHEMICAL POTENTIAL AND COMPRESSIBILITY OF THE SCEHL

The central densities for different drop sizes can be used to determine the compressibility of the SCEHL. The isothermal compressibility K_T is given by[41]

$$K_T^{-1}=2n^2f'+n^3f''=n^2\mu' , \tag{35}$$

where the pair free energy f and the chemical potential $\mu=f+nf'$ are measured with respect to the conduction band, and the prime indicates differentiation with respect to density. Thus, the compressibility is obtained from the density dependence of the chemical potential. The chemical potential is in turn obtained from $n(0,R)$ using Eq. (24):

$$\mu(n(0,R,T),T,\sigma_m)=\mu(n_0(T),T,\sigma_m) +\alpha_{\text{spec}}R^2 . \tag{36}$$

We used two methods to obtain drop radii R from the data. For large drops, the diameter was obtained from the coordinates of the points where the density profiles went to zero, with an appropriate correction for the finite slit width. For smaller drops, R was obtained from W_s using the relationship expected for the actual α_{spec} and slit width. Our experimental results, then, provide a measurement of $\mu(n)$ which can be compared directly with

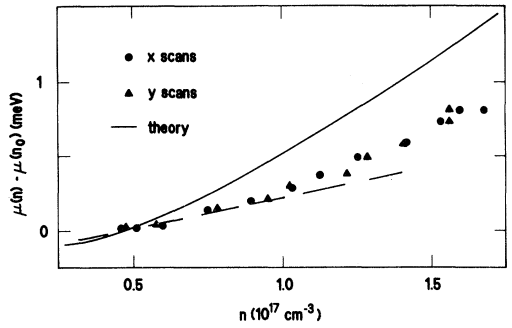

FIG. 22. Chemical potential difference vs density, using the results of two sets of data. Solid curve: theory. Dashed line: used to obtain the compressibility, as discussed in the text.

the many-body theories used for the correlation energy of electron-hole pairs.

The chemical potential difference obtained from the data is shown along with theory (the solid curve) as a function of density in Fig. 22. While the general trends are similar, the discrepancy is greater than the experimental uncertainty and appears rather serious: Over the density range $n=0.5$ to 1.5×10^{17} cm^{-3} the measured chemical potential changes by ~0.4 meV less than the calculated chemical potential (~0.7 meV compared to ~1.1 meV). Let us suppose, however, that the discrepancy occurs entirely in the exchange-correlation energy. The change in μ_{excor} in the above density range is ~2.85 meV, so the relative error is reduced. A theoretical exchange-correlation energy with a slightly steeper density dependence would agree more closely with the data. The change that would be required is approximately the difference between the zero- and infinite-stress exchange-correlation energies of Vashishta *et al.*[56,66] considered in Ref. 41.[67] We note further that these three exchange-correlation energies can all be considered representations of a universal form independent of band-structure details. Thus, our measurement of $\mu(n)$ lies essentially within the uncertainty in the mathematical representation of the detailed calculations of Vashishta *et al.*

The compressibility of the SCEHL is obtained from Fig. 22 and Eq. (35). Although K_T can be determined for any density in the range for which there are data, we restrict our analysis here to the equilibrium density at the experimental temperature. We note that the measurement is accurately isothermal. We determined the derivative $d\mu(n)/dn\,|_{n_0}$ by fitting a straight line to the data points corresponding to $n\leq1.0\times10^{17}$ cm^{-3}, avoiding the curvature at higher densities. The best fit is indicated by a dashed line. We found

$$K_T^{\text{expt}}=0.067\pm0.017\ \text{cm}^2/\text{dyn} \tag{37}$$

(with $n=0.47\times10^{17}$ cm^{-3}, $T=1.9$ K, and $-\sigma=5.5$ kgf/mm^2). The quoted uncertainty includes $\pm5\%$ for the density and $\pm15\%$ for the slope $d\mu/dn$, which includes some uncertainty in the density dependence of ρ. Other calculations of ρ yield a shallower density dependence than that given in Eq. (30).[56] On the other hand, Chou and Wong[68] estimated from their uniaxial stress measurements a steeper density dependence, since their lifetimes increased more slowly than expected with decreasing density. However, in their analysis they neglected the possibility of a density-independent recombination mechanism,[12] which could also explain their data adequately with a slower density dependence for $\rho(n)$. We have used Eq. (30) in order to be specific. The effect of neglecting this density dependence entirely is to reduce K_T by $\sim15\%$.[69]

Our theoretical value for the compressibility for the same density, temperature, and stress as in the experiment is

$$K_T^{\text{theor}}=0.041\ \text{cm}^2/\text{dyn}\ . \tag{38}$$

In view of the above comments concerning the calculation of the exchange-correlation energy and because the measurement of any quantity depending on the curvature of the free energy is very difficult, we feel that the agreement between theory and experiment is satisfactory. We note that Eq. (37) represents a significant modification of our preliminary value.[13] Each factor entering the result has been carefully evaluated in the present measurement, and more data are included. Thus the present measurement should be more accurate.

Another estimate of the compressibility of the SCEHL has recently been made by Ohyama *et al.*[19] from the temperature dependence of Alfvén wave resonances. Their value, $K_T=0.023\pm0.002$ cm^2/dyn, is considerably smaller than ours. However, they did not take into account the compression of the liquid, and as a result their measurement could be substantially in error. To see how this could occur, we use their numerical example[15] of $R=300$ μm and $\alpha=11$ meV/mm^2, since the drop size was not measured directly. The measurements were obtained 1140 μsec after cutoff of the light, and they measured a radius decay time of 1500 μsec. At the instant of the measurement,

then, we estimate $R \approx 140$ μm independent of temperature.[70] From Fig. 12 we obtain $n(0)/n_0 \approx 1.5$, which corresponds to $\beta \approx 0.5$ and $\bar{n}/n_0 \approx 1.2$. Although this increase in the average density is modest, its effect on the deduced value for K_T is greater. The quantity measured directly[19] was $\delta_n = 0.014$ deg$^{-2} = 1.89$ meV^{-2}, independent of the absolute density calibration. Now δ_n is related to the ground-state compressibility by[41]

$$K_T(n_0) = -2k^2\delta_n/[n_0^2(\gamma'(n_0))^{-1}] , \quad (39)$$

where $\gamma(n)$ is related to the heat capacity and the prime indicates differentiation with respect to density. If compression is neglected, the quantity measured, δ_n^{eff}, is related to the actual δ_n by Eq. (21b). Using the value $\beta \approx 0.5$ above, we conclude that Ohyama *et al.*[19] have underestimated δ_n by a factor of ~ 2.6 and overestimated n_0^2 by a factor of ~ 1.4. These errors *combine,* giving a deduced compressibility which is too low by a factor of ~ 3.6.[71] A more detailed comparison is not possible since the stress was not specified.

Finally, we note that the values for K_T measured for the SCEHL are considerably larger than that measured in unstressed Ge. For the latter case, Thomas *et al.*[72] measured $K_T \approx 2.3 \times 10^{-3}$ cm^2/dyn, well over an order of magnitude lower than Eqs. (37) and (38). Thus, the electron-hole liquid in stressed Ge may be nature's most compressible liquid.

IX. COMPOSITE LUMINESCENCE SPECTRA

In this section we consider the description of a luminescence spectrum from a drop containing the density distribution of Eq. (26). As discussed in Sec. V, the chemical potential μ^* measured with respect to the valence band is constant throughout the drop volume. This condition determines the form of the density distribution. Now the definition of the chemical potential is the energy required to add an electron-hole pair to the system. Spectroscopically, this corresponds to the high-energy edge of the luminescence spectrum, i.e., the Fermi level. Thus E_{spec} is also constant throughout the drop volume. A composite spectrum is a superposition of spectra for the densities contained in the drop, with the constituents having the same E_{spec}. The Fermi level shifts with drop size according to Eq. (23).

The relative intensity of the luminescence corresponding to a given density is obtained by integrating Eq. (28) over a shell with radius r and thickness dr. To describe experimental spectra, it is necessary to take into account the geometry of the experiment. In the present case luminescence was collected from a slice of width ~ 85 μm, located at the center of the drop. The constant-density spectra used to form the composites were computed using density-of-states masses appropriate for $-\sigma = 5$ kgf/mm^2.[42] In addition, the stress variation in the well was described by a uniform stress σ_m and a parabolic variation in strain energy.

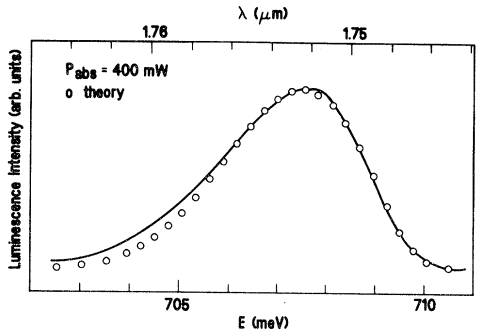

FIG. 23. Luminescence spectrum for a large drop containing a density distribution. Open circles give the theoretical composite line shape for $\alpha_{\text{spec}} = 1.6$ meV/mm^2 and $R = 800$ μm.

Figure 23 shows a luminescence spectrum measured for an excitation level of $P_{\text{abs}} = 400$ mW. The open circles are a composite spectrum computed as described above for $\alpha_{\text{spec}} = 1.6$ meV/mm^2 and $R = 800$ μm. The effects of the finite spectral resolution and the wavelength-dependent detector sensitivity were included in the calculation. The theoretical composite spectrum reproduces the experimental line shape very well.

With a satisfactory description of the lineshape for a drop containing a distribution of densities, we can quantitatively study the previously observed[11]

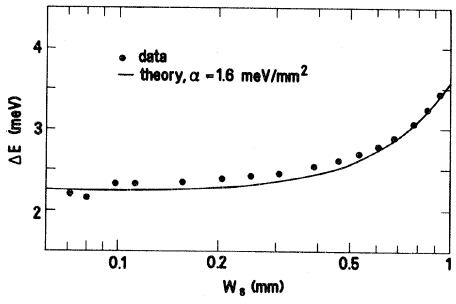

FIG. 24. Full width at half-maximum linewidth of luminescence spectra as a function of drop size. The theoretical curve is for $\alpha_{\text{spec}} = 1.6$ meV/mm^2.

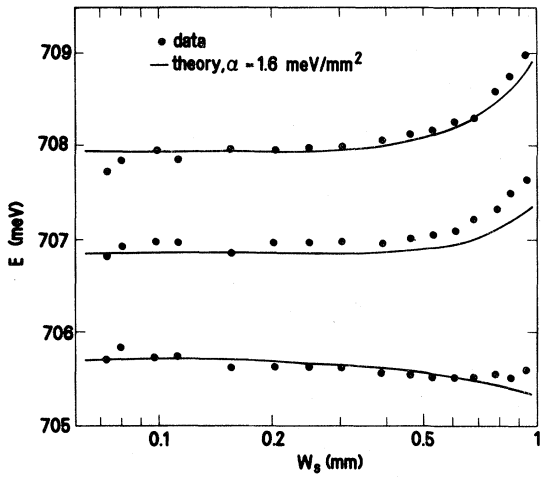

FIG. 25. Energies of peaks and low- and high-energy half-maxima of luminescence spectra as a function of drop size. The theoretical curves are for $\alpha_{\text{spec}}=1.6$ meV/mm^2.

increase in the luminescence linewidth with excitation level. In Fig. 24 we show the full width at half-maximum linewidth ΔE as a function of W_s. The spectra and slit scans were obtained using the same (side) view of the crystal. As in the previous figure, the theoretical curve is for $\alpha_{\text{spec}}=1.6$ meV/mm^2. The agreement between theory and experiment is excellent.

In Fig. 25 we consider the variation of the energy of the peaks and half-maximum points of the luminescence spectra. These features describe in more detail how the spectra broaden with increasing drop size. A striking feature of the experimental points is the quasi-invariant low-energy half-maximum point. The peak of the spectrum shifts gradually to higher energy, and the high-energy half-maximum point shifts more rapidly. Because the absolute energy of the theoretical equilibrium-density spectrum was not specified, all three theoretical curves were shifted together to give the best agreement with the data. This agreement is again excellent.

We note finally that the peak intensities of the luminescence spectra were shown as a function of drop size in Fig. 16 and also exhibit good agreement with theory. We conclude that all of the features of our measured spectra—line shapes, linewidths, relative spectral positions, and peak intensities—are described very well by composite spectra for drops having the expected and measured density distributions.

ACKNOWLEDGMENTS

I would like to thank C. D. Jeffries for his enthusiasm and support throughout this work; R. S. Markiewicz for assistance with the calculation of the stress distribution; J. E. Furneaux for cooperation in handling the data tapes; E. E. Haller for the gift of the ultrapure Ge sample and detector, and P. Vashishta for providing the results of his calculations of $\rho(n)$. This work was supported in part by the Director, Office of Energy Research, Office of Basic Energy Sciences, Material Sciences Division of the U. S. Department of Energy under Contract Number W-7405-ENG-48. I am also grateful for the hospitality at Bell Laboratories, Murray Hill, where the paper was written.

*Present address: Xerox Palo Alto Research Center, Palo Alto, California 94304.

[1]For reviews, see the articles by T. M. Rice and by J. C. Hensel, T. G. Phillips, and G. A. Thomas in *Solid State Physics,* edited by H. Ehrenreich, F. Seitz, and D. Turnbull (Academic, New York, 1977), Vol. 32.

[2]For a recent review, see Electron-Hole Droplets in Semiconductors, edited by L. V. Keldysh and C. D. Jeffries (North-Holland, Amsterdam, in press).

[3]R. S. Markiewicz, J. P. Wolfe, and C. D. Jeffries, Phys. Rev. Lett. 33, 1357 (1974); 34, 59(E) (1975).

[4]J. P. Wolfe, R. S. Markiewicz, C. Kittel, and C. D. Jeffries, Phys. Rev. Lett. 34, 275 (1975).

[5]R. S. Markiewicz, J. P. Wolfe, and C. D. Jeffries, Phys. Rev. B 15, 1988 (1977).

[6]J. P. Wolfe, W. L. Hansen, E. E. Haller, R. S. Markiewicz, C. Kittel, and C. D. Jeffries, Phys. Rev. Lett. 34, 1292 (1975).

[7]C. D. Jeffries, J. P. Wolfe, S. M. Kelso, R. S. Markiewicz, and J. E. Furneaux, J. Lumin. 12, 659 (1976).

[8]H. L. Störmer and D. Bimberg, Commun. Phys. 1, 131 (1976); D. Bimberg and H. L. Störmer, Nuovo Cimento 39B, 615 (1977).

[9]J. P. Wolfe, R. S. Markiewicz, J. E. Furneaux, S. M. Kelso, and C. D. Jeffries, Phys. Status Solidi B 83, 305 (1977); J. P. Wolfe, J. E. Furneaux, and R. S. Markiewicz, in *Proceedings of the Thirteenth Interna-*

tional Conference on the Physics of Semiconductors, Rome, 1976, edited by F. G. Fumi (Tipografia Marves, Rome, 1976), p. 954.
[10]S. M. Kelso, R. S. Markiewicz, and J. E. Furneaux, Bull. Am. Phys. Soc. 22, 269 (1977).
[11]J. P. Wolfe, R. S. Markiewicz, S. M. Kelso, J. E. Furneaux, and C. D. Jeffries, Phys. Rev. B 18, 1479 (1978).
[12]S. M. Kelso and J. E. Furneaux, Solid State Electron. 21, 1377 (1978).
[13]S. M. Kelso, *Physics of Semiconductors 1978,* edited by B. L. H. Wilson (Institute of Physics, London, 1979), p. 363.
[14]J. E. Furneaux, J. P. Wolfe, and C. D. Jeffries, Solid State Commun. 20, 317 (1976).
[15]T. Ohyama, *Physics of Semiconductors 1978,* edited by B. L. H. Wilson (Institute of Physics, London, 1979), p. 375; T. Ohyama and E. Otsuka, J. Phys. Soc. Jpn. 48, 1550 (1980).
[16]A. A. Manenkov, V. A. Milyaev, G. N. Mikhailova, and A. S. Seferov, Zh. Eksp. Teor. Fiz. Pis'ma Red. 24, 141 (1976) [JETP Lett. 24, 122 (1976)].
[17]A. G. Makarov, A. A. Manenkov, G. N. Mikhailova, and A. S. Seferov, Zh. Eksp. Teor. Fiz. Pis'ma Red. 30, 411 (1979) [JETP Lett. 30, 385 (1979)].
[18]R. L. Aurbach, L. Eaves, R. S. Markiewicz, and P. L. Richards, Solid State Commun. 19, 1023 (1976).
[19]T. Ohyama, I. Honbori, and E. Otsuka, J. Phys. Soc. Jpn. 48, 1559 (1980).
[20]T. Ohyama, A. D. A. Hansen, and J. L. Turney, Solid State Commun. 19, 1083 (1976).
[21]Ya. E. Pokrovskii and K. I. Svistunova, Zh. Eksp. Teor. Fiz. Pis'ma Red. 23, 110 (1976) [JETP Lett. 23, 95 (1976)]; *Proceedings of the Thirteenth International Conference on the Physics of Semiconductors, Rome, 1976,* edited by F. G. Fumi (Tipografia Marves, Rome, 1976), p. 849.
[22]J. C. V. Mattos, J. M. Worlock, and T. C. Damen, Solid State Commun. 22, 13 (1977).
[23]J. E. Furneaux, R. S. Markiewicz, and S. M. Kelso, Bull. Am. Phys. Soc. 22, 270 (1977).
[24]A. G. Makarov, A. A. Manenkov, G. N. Mikhailov, and A. S. Seferov, Zh. Eksp. Teor. Fiz. Pis'ma Red. 31, 440 (1980) [JETP Lett. 31, 412 (1980)].
[25]A. S. Kaminskii and Ya. E. Pokrovskii, Zh. Eksp. Teor. Fiz. Pis'ma Red. 24, 332 (1976) [JETP Lett. 24, 300 (1976)].
[26]In Si, on the other hand, the strain-confined liquid consists of a cloud of smaller drops. See P. L. Gourley and J. P. Wolfe, Phys. Rev. B 24, 5970 (1981).
[27]Ya. E. Pokrovskii and K. I. Svistunova, Zh. Eksp. Teor. Fiz. Pis'ma Red. 13, 297 (1971) [JETP Lett. 13, 212 (1971)].
[28]J. M. Worlock, T. C. Damen, K. L. Shaklee, and J. P. Gordon, Phys. Rev. Lett. 33, 771 (1974).
[29]R. S. Markiewicz, Phys. Rev. B 18, 4260 (1978).
[30]R. S. Markiewicz, Phys. Rev. B 17, 4788 (1978); R. S. Markiewicz, H. Hurwitz, Jr. and R. S. Likes, *ibid.* 18, 2780 (1978).
[31]R. S. Markiewicz and S. M. Kelso, Solid State Commun. 25, 275 (1978).
[32]W. L. Hansen and E. E. Haller, IEEE Trans. Nucl. Sci. 21, 251 (1974); E. E. Haller and W. L. Hansen, *ibid.* 21, 279 (1974).
[33]E. E. Haller, G. S. Hubbard, W. L. Hansen, and A. Seeger, in *International Conference on Radiation Effects in Semiconductors, Dubrovnik, 1976,* edited by N. B. Urli and J. W. Corbett (Institute of Physics, London, 1977), p. 309.
[34]A. D. A. Hansen, Ph.D. thesis, University of California, Berkeley, 1977 (unpublished).
[35]S. M. Kelso, Ph.D. thesis, University of California, Berkeley, 1979 (unpublished).
[36]J. E. Furneaux, Ph.D. thesis, University of California, Berkeley, 1979 (unpublished).
[37]R. S. Markiewicz, Ph.D. thesis, University of California, Berkeley, 1975 (unpublished).
[38]For $\langle 111 \rangle$ stress and a $(1\bar{1}0)$ face, one cannot define a true shear stress in two dimensions. Thus the formula is only approximate.
[39]C. Benoît à la Guillaume, M. Voos, and F. Salvan, Phys. Rev. B 5, 3079 (1972).
[40]I. Balslev, Phys. Rev. 143, 636 (1966); J. C. Hensel and K. Suzuki, Phys. Rev. B 9, 4219 (1974).
[41]S. M. Kelso, Phys. Rev. B 25, 7631 (1982).
[42]S. M. Kelso, Phys. Rev. B 25, 1116 (1982).
[43]J. C. Hensel, T. G. Phillips, and G. A. Thomas, in *Solid State Physics,* Ref. 1, p. 88.
[44]P. L. Gourley and J. P. Wolfe, Phys. Rev. Lett. 40, 526 (1978).
[45]L. D. Landau and E. M. Lifshitz, *Fluid Mechanics* (Pergamon, London, 1959), p. 230.
[46]This value is appropriate for intermediate stress in Ge. See R. K. Kalia and P. Vashishta, Phys. Rev. B 17, 2655 (1978).
[47]This value is calculated according to model 1 of Refs. 35 and 41 for a stress $-\sigma = 5$ kgf/mm^2.
[48]$\gamma(n) \sim n^{-2/3}$ is only true for parabolic bands, as discussed in Ref. 41. However, it is accurate enough for the present discussion as long as the stress does not have the critical value required to depopulate the $|M_j| = \frac{3}{2}$ valence band.
[49]This is equivalent to turning Fig. 10 on its side.
[50]See, for example, Fig. 4 of Ref. 11.
[51]C. Benoît à la Guillaume and M. Voos, Phys. Rev. B 7, 1723 (1973).
[52]B_0 is expected to change by $\sim 10\%$, for example, as the electron degeneracy changes from 4 to 1 under stress (R. S. Markiewicz, private communication).
[53]J. C. Culbertson and J. E. Furneaux, Bull. Am. Phys. Soc. 25, 268 (1980), and private communication.
[54]L. J. Schowalter, F. M. Steranka, M. B. Salamon, and J. P. Wolfe, Solid State Commun. 37, 319 (1981).
[55]P. Vashishta (private communication).
[56]P. Vashishta, P. Bhattacharyya, and K. S. Singwi,

Phys. Rev. B 10, 5108 (1974).

[57]See, for example, K. Bockasten, J. Opt. Soc. Am. 51, 943 (1961); W. L. Barr, *ibid.* 52, 885 (1962).

[58]J. C. V. Mattos, K. L. Shaklee, M. Voos, T. C. Damen, and J. M. Worlock, Phys. Rev. B 13, 5603 (1976).

[59]The authors of Ref. 22 did not observe a density variation, but this could have been obscured by the large ratio of spot size to drop diameter in the experiment.

[60]See, for example, R. Piessens, Comp. Phys. Commun. 5, 294 (1973); C. Fleurier and J. Chapelle, *ibid.* 7, 200 (1974), and references therein.

[61]R. Bracewell, *The Fourier Transform and its Applications* (McGraw-Hill, New York, 1965), pp. 262–266.

[62]I. N. Sneddon, *The Use of Integral Transforms* (McGraw-Hill, New York, 1972), pp. 210, 211, 318, and 319.

[63]Values ranging over a factor of 5 have been used by different authors (Refs. 21, 22, and 58). In addition, values of the absorption coefficient measured for unstressed Ge have been used to analyze absorption measurements in stressed Ge, while the stress dependence of the hole cross section is unknown.

[64]The curves for I_{tot} and I_{slit} have been corrected to account for the fact that the z direction is better represented by $\alpha_{\text{spec}}=4.9$ meV/mm^2 for one half and $\alpha_{\text{spec}}=1.8$ meV/mm^2 for the other half (see Ref. 35). The calculation of composite spectra is discussed in Sec. IX.

[65]The density profiles in Figs. 19 and 20 were obtained using $\rho(n)=$const in Eq. (34). Use of the density-dependent $\rho(n)$ from Eq. (30) results in a small expansion of the density scale.

[66]P. Bhattacharyya, V. Massida, K. S. Singwi, and P. Vashishta, Phys. Rev. B 10, 5127 (1974).

[67]The zero-stress (model 5) and infinite-stress (model 6) exchange-correlation energies of Ref. 41 are plotted explicitly in Ref. 35 (see Fig. 2.7 in Ref. 35).

[68]H.-h. Chou and G. K. Wong, Phys. Rev. Lett. 41, 1677 (1978).

[69]In Ref. 35 the value $K_T=0.058$ cm^2/dyn was obtained in this way.

[70]If this drop size changes with T, due for example to a change in pumping efficiency, an additional correction is required.

[71]We assume that the calculated value for $\gamma'(n_0)$ is correct, although it was not given explicitly in Ref. 19. We note, however, that γ' should be calculated for the appropriate stress and density. See Ref. 41.

[72]G. A. Thomas, T. G. Phillips, T. M. Rice, and J. C. Hensel, Phys. Rev. Lett. 31, 386 (1973).

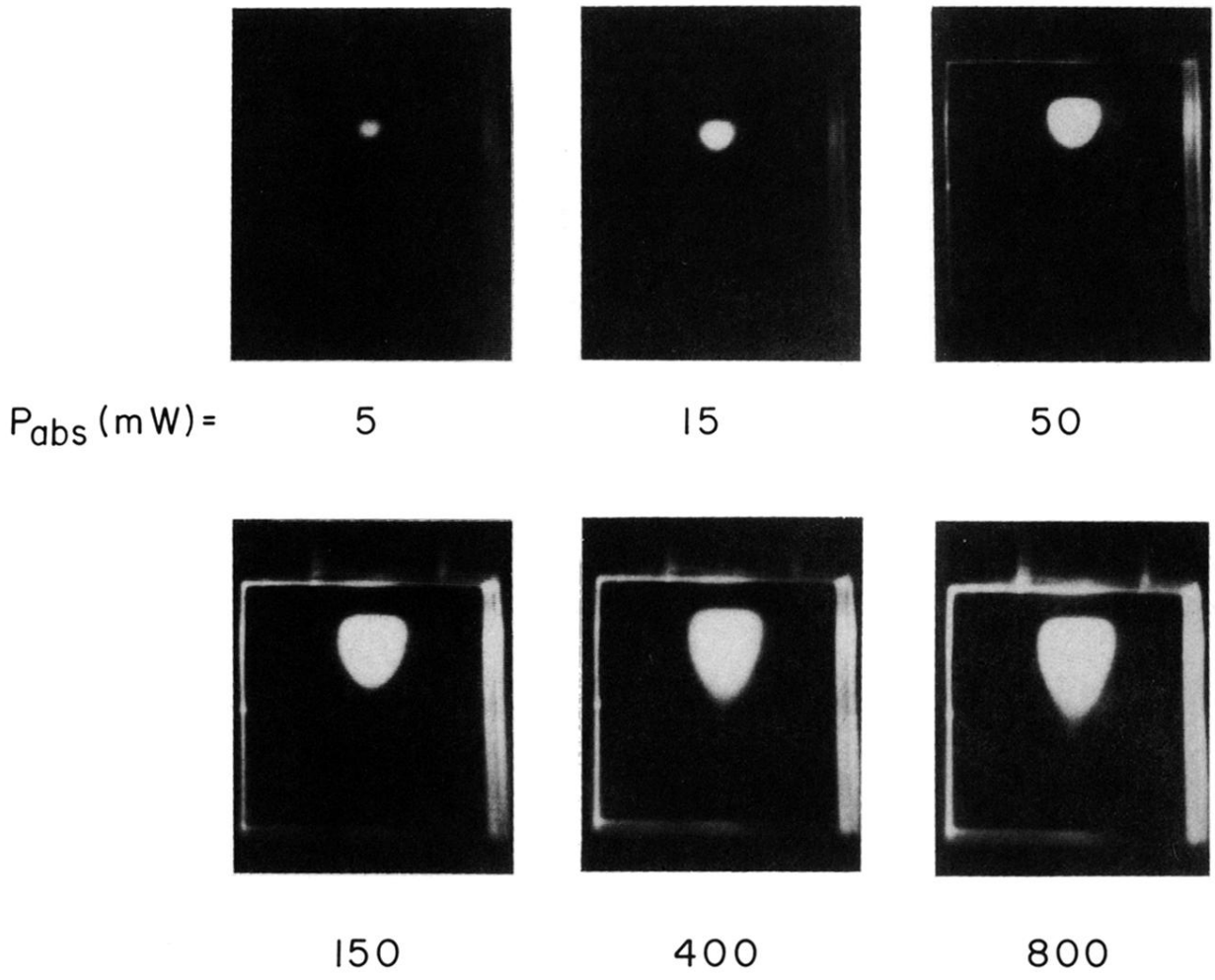

FIG. 1. Photographs of luminescence images from a Ge crystal inhomogeneously stressed in the ⟨111⟩ direction. The images are displayed using an infrared vidicon and standard television monitor (Ref. 6). The excitation levels are given by the absorbed laser power, P_{abs}. $T = 1.8$ K.